Electron Injection from Copper Diimine Sensitizers into TiO₂: Structural Effects and Their Implications for Solar Energy Conversion Devices

Michael W. Mara,[†,‡,#] David N. Bowman,[§,#] Onur Buyukcakir,[⊥,#] Megan L. Shelby,[†,‡] Kristoffer Haldrup,[∥] Jier Huang,[‡] Michael R. Harpham,[‡] Andrew B. Stickrath,[‡] Xiaoyi Zhang,[▽] J. Fraser Stoddart,[†] Ali Coskun,*[,⊥] Elena Jakubikova,*[,§] and Lin X. Chen*[,†,‡]

[†]Department of Chemistry, Northwestern University, 2145 Sheridan Road, Evanston, Illinois 60208-3113, United States

[‡]Chemical Sciences and Engineering Division and [▽]X-ray Science Division of the Advanced Photon Source, Argonne National Laboratory, 9700 South Cass Avenue, Argonne, Illinois 60439, United States

[§]Department of Chemistry, North Carolina State University, 2620 Yarbrough Drive, Raleigh, North Carolina 27695-8204, United States

[⊥]Graduate School of Energy, Environment, Water and Sustainability (EEWS), Korea Advanced Institute of Science and Technology (KAIST), Daejeon 305-701, Republic of Korea

[∥]Centre for Molecular Movies, Department of Physics, NEXMAP Section, Technical University of Denmark, 2800 Kgs. Lyngby, Denmark

S *Supporting Information*

ABSTRACT: Copper(I) diimine complexes have emerged as low cost replacements for ruthenium complexes as light sensitizers and electron donors, but their shorter metal-to-ligand-charge-transfer (MLCT) states lifetimes and lability of transient Cu(II) species impede their intended functions. Two carboxylated Cu(I) bis-2,9-diphenylphenanthroline (dpp) complexes $[Cu(I)(dpp-O-(CH_2CH_2O)_5)(dpp-(COOH)_2)]^+$ and $[Cu(I)(dpp-O-(CH_2CH_2O)_5)(dpp-(\Phi-COOH)_2)]^+$ (Φ = tolyl) with different linker lengths were synthesized in which the MLCT-state solvent quenching pathways are effectively blocked, the lifetime of the singlet MLCT state is prolonged, and the transient Cu(II) ligands are stabilized. Aiming at understanding the mechanisms of structural influence to the interfacial charge transfer in the dye-sensitized solar cell mimics, electronic and geometric structures as well as dynamics for the MLCT state of these complexes and their hybrid with TiO₂ nanoparticles were investigated using optical transient spectroscopy, X-ray transient absorption spectroscopy, time-dependent density functional theory, and quantum dynamics simulations. The combined results show that these complexes exhibit strong absorption throughout the visible spectrum due to the severely flattened ground state, and a long-lived charge-separated Cu(II) has been achieved via ultrafast electron injection (<300 fs) from the ¹MLCT state into TiO₂ nanoparticles. The results also indicate that the TiO₂-phen distance in these systems does not have significant effect on the efficiency of the interfacial electron-transfer process. The mechanisms for electron transfer in these systems are discussed and used to develop new strategies in optimizing copper(I) diimine complexes in solar energy conversion devices.
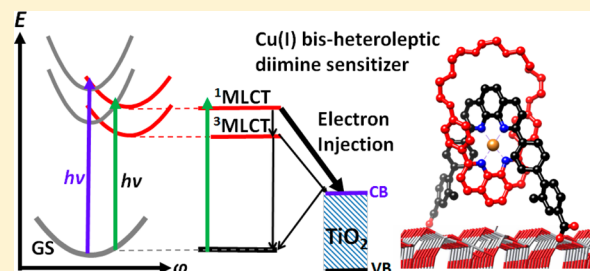
1. INTRODUCTION

The excited states of transition-metal complexes (TMCs) play important roles in solar energy conversion, such as photocatalysis for fuel generation and photosensitizers for solar cells.[1−3] So far, the most extensively used TMCs for solar energy conversion are Ru(II) [ruthenium(II)] polypyridyl complexes[4−6] as sensitizers to harvest solar photons and as electron donors from the metal-to-ligand-charge-transfer (MLCT) state,[7−10] because of their relatively high absorption coefficients in the visible region, long-lived excited states, and chemical stability. However, the drawback of such ruthenium complex-based solar energy

conversion application is the high cost and low natural abundance of the ruthenium.

Recently, there has been increasing interest in search for the replacement of Ru(II) complexes from the first-row TMCs. Some of the potential alternatives are Cu(I) [copper(I)] diimine complexes,[11−28] which exhibit similar electronic transition energies from the ground state to the MLCT state as some of the Ru(II) polypyridyl complexes. Recent examples include dye-sensitized solar cells (DSSCs) and photocatalytic systems for

hydrogen generation using derivatives of Cu(I) diimine complexes as sensitizers.[20,29−35] However, Cu(I) complexes are used far less in solar energy conversion processes than Ru(II) polypyridyl complexes because of the relatively rapid deactivation of their MLCT states via solvent quenching or irreversible photochemical reactions of the labile transient Cu(II) species.[36,37] Additionally, the MLCT state of Cu(I) diimine complexes usually undergo significant Jahn−Teller structural reorganization,[36,38−44] exhibit structure-dependent energetics,[43] possess low oxidation potentials,[37,45] and undergo excited-state quenching due to the formation of nonradiative solute−solvent "exciplexes".[14,46−52] Through previous studies we learned that the photophysical properties of the Cu(I) diimine complexes, such as lifetimes, emission quantum yields, or the intersystem crossing (ISC) rates, can be modulated by varying substituent groups on the diimine ligand, as observed by optical transient absorption (TA) and fluorescence.[29,36,38,39,41,42,53,54] In particular, the groups attached at the 2,9-position of the phenanthroline (phen) ligand can be crucial in obstructing the quenching of the MLCT state by direct solvent interaction with the transient Cu(II) center.[32,38,39,55]

The most studied Cu(I) diimine complex is copper(I) bis-2,9-dimethylphenanthroline ([Cu(I)(dmp)$_2$]$^+$, **1**),[14−16,36,41,46,49,56−61] (dmp =2,9-dimethylphenanthroline) which adopts a pseudotetrahedral, D_{2d} geometry in the ground state and exhibits the MLCT bands in the 400−500 nm spectral region, similar to those of the prototypical ruthenium trisbipyridyl complex, [Ru(II)(bpy)$_3$]$^{2+}$. The photoexcitation of **1** results in a MLCT state in which an electron from the 3d^{10} Cu(I) center is transferred to one of the dmp ligands, creating a dmp anion radical and a 3d^9 Cu(II) center. This MLCT state is then susceptible to a second-order Jahn−Teller distortion causing it to "flatten" or change the coordination from D_{2d} to D_2 symmetry, (decreasing the angle between the two dmp ligands) in <1 ps.[36,43] The resulting flattened ^{1}MLCT state undergoes an ISC to the ^{3}MLCT state with a time constant of 10−20 ps[43,57] and has enabled the transient Cu(II) center to be exposed to the solvent and to form a transient solute−solvent "exciplex" with a lower energy and shortened ^{3}MLCT state lifetime, 1.6 ns in coordinating acetonitrile and 100 ns in toluene.[36] In comparison, [Cu(I)(phen)$_2$]$^+$ with only hydrogen at the 2,9 positions is nonemissive and has a ^{3}MLCT state lifetime of 16 ps in acetonitrile ("coordinating") and 140 ps in dichloromethane ("non-coordinating").[14,36,41,42,56] The significant differences in the MLCT-state lifetimes confirm that shielding of the excited-state Cu(II) center from the solvent molecules, coordinating or noncoordinating, is necessary in order to prolong the ^{3}MLCT-state lifetimes of Cu(I) diimine complexes for solar energy conversion applications.

Substituents at 2 and 9 positions of the phen ligands do not only inhibit the flattening and the "exciplex" formation in the excited state but also alter the ground-state conformation that can, in turn, impact the excited-state properties. For example, [Cu(I)(dpp)$_2$]$^+$ (**2**) (dpp = 2,9-diphenylphenanthroline) adapts a flattened conformation in the ground state with a D_2 symmetry as a result of π−π interactions between the phenyl ring and the opposite phen ligand. Consequently, a red-shifted and broadened ground-state absorption spectrum as well as a longer excited-state lifetime were observed for **2** compared to **1**.[55] The Cu(I) coordination geometry of D_2 symmetry in **2** increases coupling between the ground state and the lowest energy ^{1}MLCT state which could not be readily accessed by **1** with a D_{2d} symmetry.[62] The phenyl groups also shield the copper center

from solvent ligation in the MLCT state, so that the luminescence lifetime is prolonged into the 100 ns range independent of the solvents and also improves the spectral coverage by extending the ground-state absorption farther into the red.

Building on the knowledge of structural factors responsible for the ground- and excited-state properties of Cu(I) diimine complexes, we constructed two new heteroleptic complexes, [Cu(I)(dpp-O(CH$_2$CH$_2$O)$_5$)(dpp-(COOH)$_2$)]$^+$ (**3**) and [Cu-(I)(dpp-O(CH$_2$CH$_2$O)$_5$)(dpp-(Φ-COOH)$_2$)]$^+$ (**4**, Φ = tolyl) (see Figure 1). They are specifically designed to simultaneously
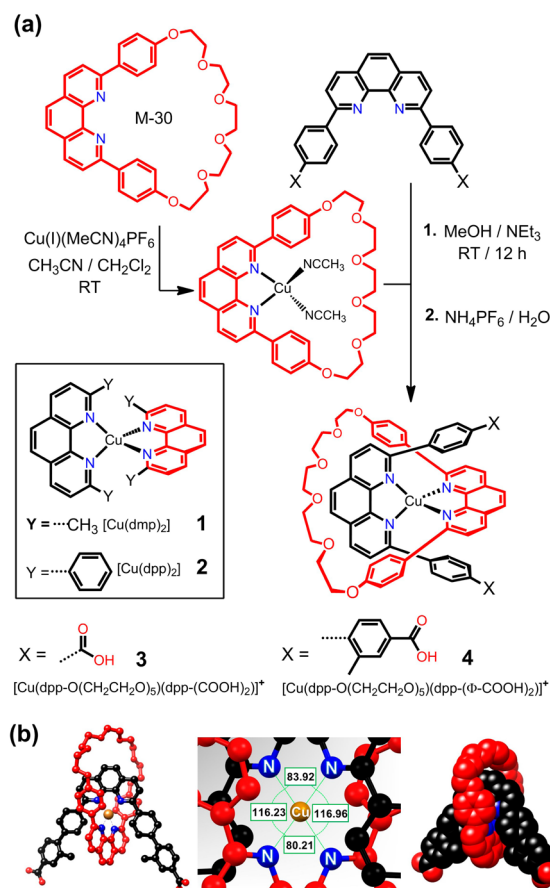

Figure 1. Structural formulas of the Cu(I) dimine complexes, copper(I) bis-2,9-dimethylphenanthroline {[Cu(I)(dmp)$_2$]$^+$, **1**}, copper(I) bis-2,9-diphenylphenanthroline {[Cu(I)(dpp)$_2$]$^+$, **2**}, and (a) the synthesis of the heteroleptic Cu(I) diimine complexes: [Cu(I)(dpp-O-(CH$_2$CH$_2$O)$_5$)(dpp-(COOH)$_2$)]$^+$ **3** and [Cu(I)(dpp-O-(CH$_2$CH$_2$O)$_5$)(dpp-(Φ-COOH)$_2$)]$^+$ **4**. (b) Ball-and-stick and space-filling representations of the crystal structure of **4**, along with the corresponding N−Cu−N angles.

possess several desirable properties: (1) long-lived ^{3}MLCT state, (2) prolonged ^{1}MLCT-state lifetime to gain a higher driving force for the electron injection, (3) chemical stability in the excited state, and (4) stable attachment to TiO$_2$ nanoparticle. Important structural features of these complexes include phenyl groups substituted at 2,9 positions of the phen ligands that shield the Cu(I) center from solute−solvent interactions and lead to flattened ground-state conformation, thus achieving longer-lived ^{1}MLCT and ^{3}MLCT states. The catenane chain hinders the potential dissociation of the transient Cu(II) species, resulting in more robust complexes than other copper bis-phen complexes.

Finally, carboxylic acid groups serve as anchoring groups for attachment of **3** and **4** to the TiO$_2$ nanoparticle surface.

Optical TA measurements and quantum dynamics simulations were performed to determine how quickly electrons transfer into TiO$_2$. X-ray transient absorption (XTA) measurements were performed to determine what structural changes occur between the ground and excited states and whether the exited-state structure differs before and after charge transfer into TiO$_2$. These results help to further lay the groundwork for the development of low-cost abundant copper complexes for DSSCs and other photochemical applications.

2. EXPERIMENTAL SECTION

2.1. General Procedure. For the synthesis of [Cu(I)(dpp-O(CH$_2$CH$_2$O)$_5$)(dpp-(COOH)$_2$)]$^+$, **3**, and [Cu(I)(dpp-O-(CH$_2$CH$_2$O)$_5$)(dpp-(Φ-COOH)$_2$)]$^+$, **4**: [Cu(MeCN)$_4$]PF$_6$ (1 equiv) was dissolved in predegassed MeCN and stirred under N$_2$ atmosphere at room temperature until a clear solution was obtained. Using a double-ended transfer technique, [Cu(MeCN)$_4$]PF$_6$ solution in MeCN was added under an N$_2$ atmosphere to a stirred solution of M-30 (1 equiv) in CH$_2$Cl$_2$ at room temperature, affording a dark orange solution. When this solution was added to a solution of corresponding thread components (1 equiv) in MeOH containing Et$_3$N (3 equiv), instantaneous formation of a dark red solution was observed, indicating the formation of the [Cu(I)(dpp-O(CH$_2$CH$_2$O)$_5$)(dpp-(COOH)$_2$)]-PF$_6$, **3**, and [Cu(I)(dpp-O(CH$_2$CH$_2$O)$_5$)(dpp-(COOH)$_2$)]PF$_6$, **4**, pseudorotaxanates. The mixture was then stirred for 12 h at room temperature under N$_2$ atmosphere. Afterward, it was concentrated under reduced pressure, before being dissolved in the minimum amount MeOH and added to a saturated aqueous solution of NH$_4$PF$_6$ at pH 3.5, affording a dark red solid. The solids were filtered on sintered glass to give the crude product, which was purified by column chromatography on silica gel, affording the pure pseudorotaxanates **3** and **4**. Synthesis of precursors and more experimental details can be found in the Supporting Information (SI).

2.2. Optical Ultrafast TA Measurements. Optical TA measurements were performed with an apparatus based on an amplified Ti-Sapphire laser system as described earlier.[32] The excitation wavelength was at 415 nm. The instrument response function of the apparatus is about 200 fs (fwhm). The data acquisition was achieved using a Helios system (Ultrafast Systems).

2.3. Optical Nanosecond Transient Absorption Measurements. Samples were excited at 530 nm using output of an optical parametric oscillator pumped with third harmonic of a Nd:YAG laser (Surelite-II, Continuum). The width of the pump pulses was approximately 5 ns. Single wavelength kinetic traces were obtained using a Xe flash lamp ($\tau \sim 50~\mu s$) as a probe source, Triax-180 monochromator (Horiba Jobin Yvon), and a PMT with its output digitized with an Agilent DSO6054A oscilloscope. The instrument response time was about 10 ns. The details were described in.[32]

2.4. XTA Measurements. The experimental setup at beamline 11-ID-D of the Advanced Photon Source used for the XTA measurements has been described elsewhere.[63−67] The excitation laser pulse has 0.75 mJ/pulse at 527 nm with 1 kHz repetition rate, which was focused to a 1 mm^2 spot size on the sample. **3** and **4** were dissolved in methanol at 2 mM for solution-phase measurements, and ∼1 mM samples were mixed in methanol with Degussa P25 TiO$_2$ to prepare the TiO$_2$-bound samples. Time delay scans were performed at set X-ray energies by varying the delay of the laser relative to the synchronized X-ray bunch via an electronic delay. HPLC tubing of length 10 cm was used to establish a fast laminar flow (a nozzle with a diameter of 0.7 mm, a flow rate of ∼50 mL/min) which allows fresh sample volumes to be excited by consecutive laser pulses at 1 kHz repetition rate; TiO$_2$-bound samples were flown as a suspension.

2.5. Computational Methodology. *2.5.1. Molecular Structure and Absorption Spectra.* To simplify the study of complexes **3** and **4**, the catenate chain was replaced by capping hydrogens. These simplified complexes are labeled as **3′** and **4′** in the further discussion. The catenate

chain is unlikely to significantly impact the central coordination environment, attachment of the Cu(I) diimine complexes to the semiconductor surface, or the photophysical properties of their chromophore-semiconductor assemblies. Additionally, the catenate chain adds a large number of degrees of freedom to the system, leading to an overly complicated potential energy surface and computationally expensive optimization.

Singlet ground states for complexes **1**, **2**, **3′**, **4′**, and [Cu(I)(dpp-COOH)(dpp)]$^+$ (dpp-COOH = 2,9-diphenyl-1,10-phenanthroline-X-carboxylic acid, with X = 4 or 5) were optimized in vacuum at the B3LYP[68,69] level of theory, with Grimme's dispersion correction term D2.[70] The SDD effective core potential and associated basis set[71] were used for the Cu center, and the 6-31G* basis[72,73] was utilized for all other atoms. Optimized structures of the lowest-lying ^{3}MLCT states were also obtained for complexes **3′**, **4′**, and [Cu(I)(dpp-COOH)-(dpp)]$^+$ at the same level of theory, but employing the polarizable continuum model (PCM) in the optimization,[74] with methanol as the solvent. Hybrid functionals, such as B3LYP, are known to provide accurate geometries for first-row transition-metal complexes[75] as well as more accurate UV−vis spectra than the pure functionals.[76] While inclusion of the solvent effects via the PCM does not significantly influence the structure optimizations in the ground state, it has been shown to impact the structure as well as electronic-state localization in the excited state.[77]

Time-dependent density functional theory (TD-DFT),[78−80] with the same basis set and functional as used for the structure optimizations, was employed to obtain 30 lowest excitation energies in the UV−vis region of the absorption spectrum for complexes **1**, **2**, **3′**, and **4′**. Solvent effects were introduced via the PCM, employing methanol as the solvent. The absorption spectra were simulated by convoluting the spectrum composed of the δ-functions at the excitation energies times the oscillator strengths with a Lorentzian line-shape with the half-width at half-maximum (hwhm) equal to 0.2 eV. The hwhm was chosen so as to achieve the best match between the experimental and calculated spectra. The canonical Kohn−Sham (KS) orbitals of the ground state were used to characterize the most intense transitions ($f_{osc} > 0.0075$) in the visible portion of the spectra ($\lambda > 350$ nm). The Gaussian 09 software package was used for all molecular calculations.[81]

2.5.2. Slab Model Optimization. The Vienna Ab Initio Simulation Package (VASP)[82−85] was utilized to optimize bulk anatase and a slab model for the anatase (101) surface using the PBE functional[86,87] with the projector augmented wave method.[88] The PBE functional was chosen for its reduced computational cost in comparison to hybrid functionals. Details of the computational parameters can be found in the SI.

The optimized structures of benzoic acid and *m*-toluic acid on the anatase (101) surface were used to perform constrained optimizations of complexes **3′** and **4′**, respectively, keeping the linker and the lower half of the aryl ring (three carbon and two hydrogen atoms) frozen at surface geometry. Calculations were done with the Gaussian 09 software package at the B3LYP/SDD, 6-31G* level of theory in vacuum. Following the constrained optimization, complexes **3′** and **4′** were aligned onto the surface using the linker geometry as a reference.[89]

2.5.3. Interfacial Electron-Transfer Simulations. Interfacial electron transfer (IET) was modeled employing quantum dynamics simulations[90−96] on the **3′**-TiO$_2$ and **4′**-TiO$_2$ assemblies. This method has been successfully employed in the past to estimate rates for IET as well as explain experimental trends.[91−97]

The time-dependent electronic wave function was propagated according to the extended Hückel (eH) Hamiltonian. Initial states for the IET simulations were selected based on the ^{1}MLCT states from TD-DFT calculations, by matching the virtual eH orbitals to the KS orbitals populated by the visible light excitations. For the ^{3}MLCT structures, the donor states were determined by matching the eH virtual orbitals to the singly occupied natural orbitals (SONOs) obtained from the DFT calculations. Details of the eH parametrization and quantum dynamics methodology can be found in the SI.

3. RESULTS

3.1. The Synthesis and Characterization of 3 and 4. The synthetic pathway for the preparation of Cu(I) diimine complexes **3** and **4** is summarized in Figure 1a. These copper complexes, which are in the form of [2]pseudorotaxanates, were synthesized by following Cu(I)-templated "gathering-and-threading" strategy.[98] The Cu(I) metal center serves as the gathering and templating agent, while threading the axle unit through the ring structure. As depicted in Figure 1a, the coordinating ring (M-30) was first treated with [Cu(MeCN)$_4$]-PF$_6$ in stoichiometric amounts and followed by the addition of corresponding carboxyphenyl-substituted phenanthrolines to form highly stable heteroleptic bischelate complexes, **3** and **4** (see SI for details.) Dark red single crystals of **4·Cl** were grown by slow diffusion of Et$_2$O into MeOH solution of **4·Cl**. Ball-and-stick and space-filling representations of the solid-state super-structure of **4·Cl** are given Figure 1b. The crystal occupies a monoclinic crystal system with the space group $P2(1)/n$. [Note: Single crystal data for Cu(I)(dpp-O(CH$_2$CH$_2$O)$_5$)(dpp-(Φ-COOH)$_2$)]$^+$: C$_{79}$H$_{82}$ClCuN$_4$O$_{15}$, red plate crystals, F.W. = 1426.48, crystal size 0.41 × 0.17 × 0.04 mm, monoclinic, space group $P2(1)/n$, a = 12.7999(6), b = 15.1536(8), c = 36.6914(18) Å, β = 94.913(3)°, V = 7091.1(6) Å^3, Z = 4, calculated density = 1.336 g cm^{-3}, T = 100(2) K, R_1 ($I > 2\sigma(I)$) = 0.1436, wR_2 = 0.3309. CCDC 1062171 contains the supplementary crystallographic data for **4·Cl**. These data can be obtained free of charge from The Cambridge Crystallographic Data Centre via (www.ccdc.cam.ac.uk/data_request/cif)]. The Cu–N bond lengths were found to be in the range of 2.050 to 2.064 Å, which are typical for these types of Cu complexes. The N–Cu–N angles are, however, are significantly distorted from ideal tetrahedral geometry and lie between 80.21 and 116.96°.[99] This characteristic angle distortion is typical and one of the distinctive features for this type of Cu(I) complexes.[100] This distortion not only allows more efficient packing but also enables efficient [$\pi^{...}\pi$] stacking interaction between phenoxy substituent of the ring component (M-30) and the phenanthroline core of the axle unit.

The pseudorotaxanates, **3** and **4**, were characterized by mass spectrometry (ESI-HRMS, see SI) and also by one- and two-dimensional NMR spectroscopy. The ^{1}H NMR spectra of complexes are shown in SI. The formation of pseudorotaxanates led to a drastic upfield shift for the *ortho* (H$_1$) and *meta* (H$_2$) protons of phenyl groups of the ring component (M-30). Since, these protons are affected by the ring current of phenanthroline core, their resonances appear at a higher field.[101,102] Similarly, H$_d$ and H$_e$ protons of the axle also show an upfield shift. These findings are supported by the X-ray crystal structure of **4·Cl**, which shows the positioning of protons H$_1$, H$_2$, H$_d$, and H$_e$ in the shielding zone of the phenanthroline core. We have also observed a slight upfield shifts for the methyl groups and the H$_g$ protons of **4**.

3.2. UV–vis Spectral Features and Their Assignments. The UV–vis spectra of **1–4** (Figure 2) show two main features in the 350–750 nm region: a main peak around 440 nm and a broader shoulder extended into the red, both assigned to the MLCT transitions. The shoulder feature has been assigned to S$_0$ to S$_1$ transition in the flattened coordination geometry, while the 440 nm feature originates from S$_0$ to S$_2$ transitions.[38,53,59,100] An increase in extinction coefficient for the shoulder feature indicates an increased flattening of the ground state compared to **1**,[38,39,53] as seen in the spectra of **2–4** where the steric hindrance of the two bulky phenyl groups at the 2,9 positions
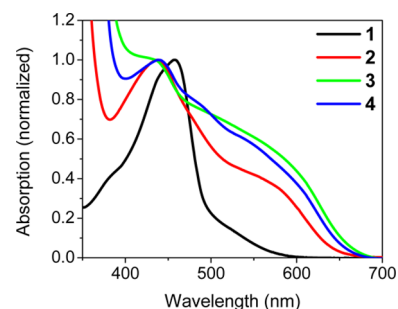

Figure 2. UV–vis spectra of **1–4** in acetonitrile.

cause the flattening to accommodate π-orbital interactions between the phenyls and phenanthroline. In comparison, **3** and **4** absorb even more in the shoulder region than **2**, indicating that a flattened geometry is enforced in them, while the absorption peak positions are largely unchanged. The assignment of the fine structures within the shoulder feature is currently unclear, which may arise from the minor difference between the two diimine ligands.

3.3. Ultrafast Excited MLCT-State Dynamics. The optical TA spectra of **4** under the 415 nm excitation in solution are shown in Figures 3 and 4, while the corresponding results for **3**
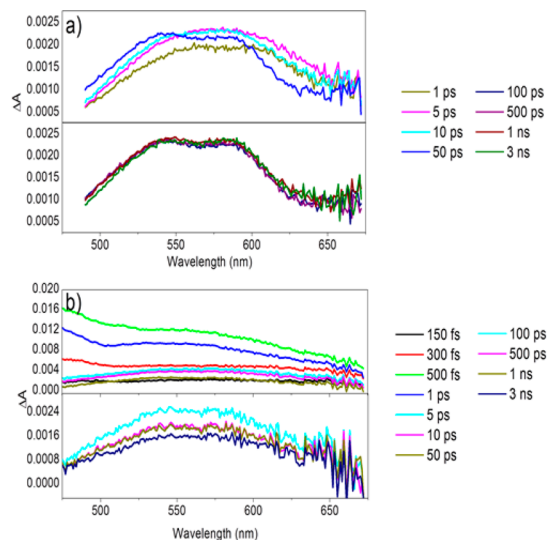

Figure 3. TA spectra of **4** in solution (a) and attached to TiO$_2$ (b).

are shown in the SI. The time constants (τ's) for the global multiexponential fits of the kinetics traces are shown in Table 1. Within 1 ps after the excitation, the TA spectrum of **4** exhibits a broad and featureless band that then evolves in ~10 ps into a narrower band with two humps similar to those of **1** and **2** and assigned as the vibronic bands of the radical anion formed in one of the two ligands via the MLCT transition.[58,103] Meanwhile, the spectrum blue-shifts due to the ISC to form the ^{3}MLCT state.[36,39] From 10 ps delay then on, the spectral shape remains largely unchanged in the 3 ns time window of the TA measurements which agrees with its 100 ns lifetime of the ^{3}MLCT state measured by the nanosecond photolysis apparatus to be described later.

In contrast, the TA signal amplitude and shape in the 500–650 nm region for the **4**-TiO$_2$ hybrid are significantly different from those of **4** in MeOH (Figure 3b). The double hump features are no longer recognizable, and the absorption peak appears to be
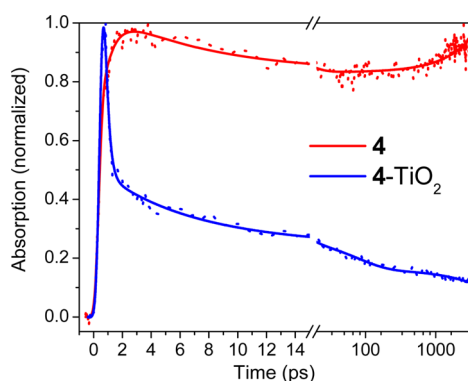
Figure 4. Excited-state absorption kinetics of **4** under 415 nm excitation probed at 600 nm where only the signals from the MLCT state are present because the ground-state bleach and Cu(II) species absorption cancel each other.

Table 1. Time Constants of the Excited-State Dynamics from the Global Fitting (Excitation at 415 nm)[a]

	3	**3**-TiO$_2$	**4**	**4**-TiO$_2$
τ_1 (ps)	0.6 (rise)	<0.3	0.6 (rise)	<0.3
τ_2 (ps)	10.6	5.1	11.1	6.0
τ_3 (ps)	>3000	81.1	>3000	76.8
τ_4 (ps)	–	>3000	–	>3000

[a] τ's are time constants of the exponential components respectively obtained from the global fits; **3** and **4** were measured in methanol with their τ_1's as the rise time constants respectively, while others are all decay components.

broadened due to photoinduced interfacial electron injection that quenches the MLCT state and hence reduced the excited-state absorption as seen previously in the hybrid of [Cu(I)-(dppS)$_2$]$^+$ (dppS = diphenyl-disulfonate) and TiO$_2$ nano-particle.[32,40]

The precise assignments in this spectral region are difficult due to the spectral congestion of the MLCT-state absorption and ground-state bleach as well as charge-separated Cu(II) species absorption. The reaction kinetics are modeled by multiple exponential functions, and the time constants were extracted via a global fitting procedure where they are constraint across the TA spectra, which resulted in three time constants (Table 1). A ~600 fs rise time was assigned to the Jahn−Teller distortion, consistent with previous results from the other [Cu(I)(phen)$_2$]$^+$ derivatives studied so far.[36,43] The kinetics also exhibited ~11 ps decay time constant, attributed largely to the growth of the ^{3}MLCT state through ISC which gave a rise of the apparent blue shift of the excited-state absorption.

In order to map out the dynamics of the charge injection, we selected a wavelength range near 600 nm where optical densities for the ground-state bleach and the charge-separated Cu(II)-state absorption are nearly equal as observed in spectroelec-trochemical measurements.[32] Figure 4 displays excited-state absorption kinetics traces for **4** in methanol and **4**-TiO$_2$ probed at 600 nm, corresponding to the excited-state absorption spectra (Figure 3a). The small spectral region around 600 nm is where the ground-state bleach and charge-separated species Cu(II) absorption cancel each other, leaving the contributions only from the MLCT-state absorption.

The distinctively different kinetics trace for **4** and **4**-TiO$_2$ at 600 nm (Figure 4) indicate that **4**-TiO$_2$ exhibits a quick depletion of the excited state in <300 fs, similar to that observed for

[Cu(I)(dppS)$_2$]$^+$ attached to TiO$_2$.[32,40] Based on the relative fraction of the <300 fs component to the longer time constant components, both **3**-TiO$_2$ and **4**-TiO$_2$ exhibit very similar yields and rates of the IET, despite the difference in the linker lengths that define the distance between the ligand and the TiO$_2$ nanoparticle surface. The implications of this will be discussed later. There are also decay lifetimes of 6.0 and 76.8 ps which may correspond to the ISC of the remainder MLCT state and the IET from the ^{3}MLCT state. The 6.0 ps time constant, while consistent with the ISC time constant measured for the solution-phase sample, likely does not correspond to ISC since there is no blue-shift in the TA spectrum. Therefore, this time constant may represent charge recombination from the TiO$_2$ to the nominally Cu(II) complex. Finally, there is a time constant ≫3 ns, which likely corresponds to the excited-state decay of **4** that did not transfer an electron into TiO$_2$.

3.4. Excited-State and Electron-Transfer Kinetics on the Nanosecond Time Scale. Based on the UV−vis spectra shown in Figure 2 and a previous spectroelectrochemistry measurement,[32] only the MLCT state and Cu(II) after IET can contribute the TA signals at 700 nm on the time scales of nanosecond and longer. Nanosecond photolysis kinetics measurements were carried for **3** and **4** as well as their hybrids with TiO$_2$ with 532 nm excitation. The data for **4** and **4**-TiO$_2$ are shown in Figure 5 (the data for **3** and **3**-TiO$_2$ are in the SI).
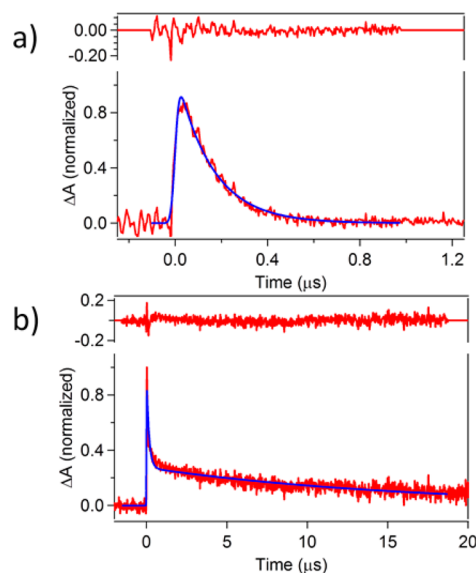

Figure 5. Nanosecond TA kinetics probed at 700 nm following 530 nm excitation. Top: **4** in methanol; and bottom: **4**-TiO$_2$.

The time constants and pre-exponential factors from the multiexponential kinetics fits are shown in Table 2. Both photoexcited **3** and **4** in methanol show monoexponential decay kinetics with a 150 ns time constant, which is similar to the triplet MLCT-state lifetime of 2,9-aryl-substituted copper bis-phen with the solvent access to the copper center in the excited state effectively blocked.

In presence of IET, the photoexcited **4**-TiO$_2$ exhibits a biexponential decay kinetics at 700 nm, with time constants of ~150 ns and >10 μs. Compared to the kinetics of **4** in MeOH, the 150 ns decay kinetics is clearly attributed to those ^{3}MLCT-state molecules that do not undergo the IET, whereas the >10 μs component is attributed to the Cu(II) species generated by the charge separation. Although the Cu(II) species occurs in both

Table 2. Nanosecond Optical TA Multiexponential Fit Parameters[a]

	3	3-TiO$_2$	4	4-TiO$_2$
τ_1 (ns)/A_1 (%)	150	150(76)	150	150(71)
τ_2 (μs)/A_2 (%)	–	>10(24)	–	>10(29)

[a]700 nm probe; τ's and A's are time constants and relative fractions (in parentheses) of the exponential components respectively obtained from the fits; **3** and **4** were measured in methanol with their τ_1's as the rise time constants respectively, while others are all decay components; the time resolution is ∼10 ns.

the MLCT state and the charge separate state, the signal beyond 1 μs delay is clearly only due to the Cu(II) species, which is also shown in the XTA results discussed later. If the absorption coefficients for the Cu(II) species in the MLCT state and charge separate state are the same at 700 nm, one can estimate that ∼30% of the MLCT triplet excited state achieved sustained the long-lived charge separate state from the electron injection into TiO$_2$. The discrepancy is likely due to the charge recombination processes to be investigated in the future. The ratio between the excited state and charge-transfer state will be further discussed based on the XTA results in the following section.

3.5. Excited-State and Charge-Separated State Structures by XTA Measurements. As one can see from the optical TA results, it is uneasy to verify the Cu(II) species due to the overlap of optical signatures from different species in the same region. In order identify the intermediates and structural factors that are important in IET dynamics, we also monitored electronic and nuclear structural evolution around the copper center for **3** and **4** and their TiO$_2$ hybrids by XTA measurements at the copper K-edge. X-ray absorption near edge structure (XANES) spectra of **4** in MeOH and **4**-TiO$_2$ in the ground state and within 100 ps of the excitation are shown in Figure 6A,B. The ground-state XANES spectra of **4** are almost identical with those of its root complex **2** showing a distinct 1s → 4p$_z$ transition peak at
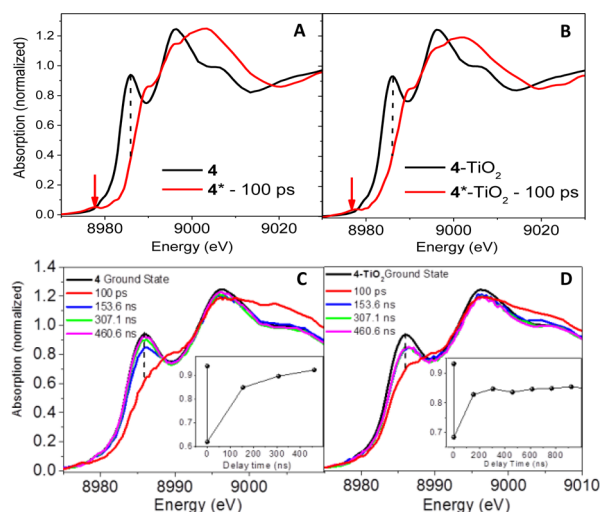

Figure 6. XANES spectra of **4** in MeOH (A) and **4**-TiO$_2$ (B) of the ground state (black) and photoexcited state at 100 ps time delay (red) with the ground-state contributions removed (the red arrows indicate a pre-edge feature arising due to the Cu(II) 3d^9 as a result of the MLCT transition). The XANES spectra at different delay times for **4** (C) and **4**-TiO$_2$ (D) where the insets represent the time evolution of the peak intensities at 8986 eV (the peak of the 1s → 4p$_z$ transition). The time windows are 500 ns for (C) and 1000 ns for (D).

8986 eV, a characteristic feature in the Cu(I) diimine complexes.[104] In comparison, lower amplitude of the corresponding peak in **1** was observed. From the energy-minimized structure calculated by the DFT calculations, the ground-state structures of **2**−**4** can only form flattened tetrahedral coordination, while that of **1** stabilizes at a pseudotetrahedral coordination with the two orthogonal ligand planes. Hence, the amplitude of the 1s → 4p$_z$ transition peak increases with the degree of the distortion from pseudotetrahedral coordination geometry.[42,104,105]

The XANES spectra of the photoexcited **4** and **4**-TiO$_2$ in Figure 6A,B were extracted by subtracting the remaining ground-state contribution from the spectrum of the laser excited sample. The fractions of the remaining ground state were determined by modeling the XANES spectra with a linear combination of the XANES spectra of the reference complexes [Cu(I)(dpp)$_2$]$^+$ and [Cu(II)(dpp)$_2$]$^{+2}$ in the region from −20 to +30 eV about Cu K-edge. A shift of the edge energy of ∼3 eV from 8983.5 eV for the Cu(I) species to 8986.5 eV for the Cu(II) species was observed, similar to the previously observed XANES spectra of the Cu(II) species and hence indicative of the oxidation of Cu(I) to Cu(II). Compared to the ground state, the 1s → 4p$_z$ peak in the photoexcited species also shifts from 8986 to 8989 eV along with significantly altered multiple scattering features (Figure 6A,B). A new pre-edge peak appears at 8978 eV which was previously assigned as a quadrupole-allowed 1s → 3d transition which only occurs when there is a vacancy in 3d orbitals as in 3d^9 or Cu(II).[104] The XANES spectra for the ground-state complex in solution and attached to TiO$_2$ appear to be virtually identical, indicating that this complex likely retains the same structure in the ground state in each case.

Based on the above observation, it is established that the intensity variation at the 1s → 4p$_z$ peak energy (8986 eV) can be used to follow the dynamics of the copper oxidation-state change during the excited-state processes. The ground state should have the highest intensity, and the excited state at the time delay of 100 ps should have the lowest intensity. With the delay time increases, the system should gradually recover back to the intensity level of the ground state. The inset in Figure 6C shows a ∼150 ns ground-state recovery kinetics agreeing with the excited-state lifetime constant from the TA results, while that in Figure 6D shows only a partial recovery due to approximately 30% long-lived charge separate Cu(II) species as long as 3.38 μs, confirming the IET process as observed in Figure 5.

In order to determine structural details around the copper center, the extended X-ray absorption fine structure (EXAFS) spectra at Cu K-edge were analyzed. Figure 7 displays the Fourier transformed EXAFS spectra of the ground state **4** in methanol and on TiO$_2$ (k = 2.55−7.55 Å$^{−1}$). The structural parameters extracted from the fitting using IFEFFIT[106,107] are listed in Table 3. Although Cu−C−C multiple scattering contributions from the phenanthroline ligand were included in the fits, these paths are not shown here. A description of the scattering paths used for the fit is depicted in Scheme 1. As shown in Table 3, the structural details for **4** in solution and on TiO$_2$ are almost identical within the experimental errors. It should be noted that the secondary phenyl rings directly attach to TiO$_2$ through the −COOH groups and are too far from the copper center, and hence their structural details are beyond the EXAFS detection range. However, the distances from the copper center to the atoms on the first phenyl can be obtained. The ground-state structures of **3** and its hybrid are almost the same with those of **4** and are shown in the SI. Also obtained through the fitting is the 3.16 Å distance between Cu
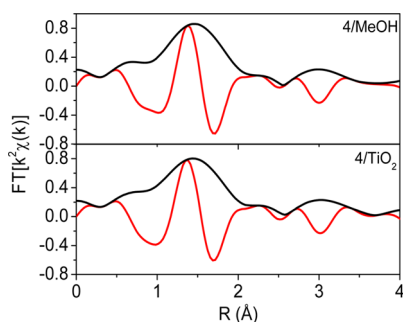
Figure 7. Fourier-transformed EXAFS spectra for **4** in methanol (top) and attached to TiO$_2$ (bottom). Amplitude (black) and phases (red) spectra are shown. The Fourier transform was performed over k range of 2.6–7.6 Å^{-1}.

Table 3. Structural Parameters for Ground State of 4[a]

scattering[b] path (CN)	distance (Å)[c]		DW factor (Å^2)[d]	
	CH$_3$OH	TiO$_2$	CH$_3$OH	TiO$_2$
Cu−N (4)	2.03	2.02	0.008	0.009
Cu−C (b) (4)	2.76	2.77	0.007	0.007
Cu−C (c) (4)	3.00	3.00	0.001	0.001
Cu−C (d) (4)	3.16	3.16	0.009	0.009
Cu−C (e) (4)	3.30	3.31	0.001	0.001

[a]S_0^2 = 1.0, ΔE = 3.0 eV. [b]Coordination number in parentheses. [c]± 0.02 Å. [d]Debye−Weller factor or σ^2.

Scheme 1. Atom Labels Used in XAS Data Fitting[a]
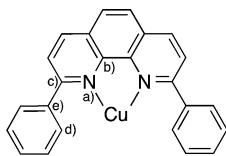
[a]Secondary phenyls and catenate chain are omitted.

and C(d), which is significantly shorter than the 3.25 Å distance measured for **2**. All these structural similarities indicate that the addition of the second phenyl rings has little effect on the inner shell structures around the copper center.

XTA measurements were also performed on the **4-TiO$_2$** hybrid to measure excited and charge separate state structures. At the 459 ns delay from the laser pump pulse, the MLCT state of **4** in solution has relaxed back to the ground state, based on the 150 ns lifetime of the ^{3}MLCT state measured in the nanosecond TA. In comparison, the Cu(II) species of **4-TiO$_2$** after the charge injection to the TiO$_2$ has a much longer decay time constant of >10 μs. Therefore, the XTA spectrum of **4-TiO$_2$** hybrid collected at 100 ps (after removal of the ground-state spectrum) is from a mixture of two species: the excited state **4** injected an electron into TiO$_2$, and that did not inject an electron. At a much longer time delay, e.g., >300 ns, only those Cu(II) species resulting from the interfacial electron injection would remain, which is an important piece of evidence to prove the electron injection into TiO$_2$. Here, the spectrum at the 100 ps delay will be referred to as the photoexcited-state spectrum, while spectra collected after 300 ns delay will be referred to as the charge transfer-state spectra. Since the XTA measurements were carried out using an X-ray pulse train with time interval of 153.5 ns, signals from X-ray pulses delayed from the laser pulse by 0.46 to 3.38 μs were averaged for the charge-transfer spectrum. Some of the Cu(II)

species resulting from electron injection into the TiO$_2$ likely undergoes fast charge recombination, as shown by the ultrafast optical TA measurements. However, this contribution to the spectrum will be removed during the ground-state subtraction in preprocessing and therefore will not have an impact on the results.

The XTA spectra of **4-TiO$_2$** are shown in Figure 8. Structural parameters resulted from the fits are shown in Table 4 (as before,
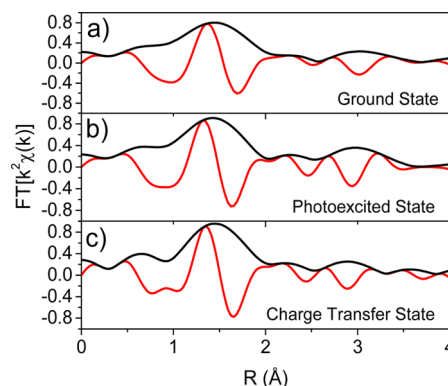

Figure 8. Fourier-transformed EXAFS spectra for **4-TiO$_2$** hybrid in (a) the ground state, (b) excited state, and (c) charge-transfer state. Amplitude (black) and phases (red) spectra are shown. The Fourier transform was performed over k range of 2.6–7.55 Å^{-1}.

Table 4. XAS Fitting Parameters for 4-TiO$_2$[a]

scattering[b] path (CN)	distances (Å)[c]			DW factors (Å^2)[d]		
	grd. state	ex. state	CT state	grd. state	ex. state	CT state
Cu−N (4)	2.02	1.97	2.00	0.009	0.007	0.005
Cu−C (b) (4)	2.77	2.77	2.78	0.007	0.009	0.007
Cu−C (c) (4)	3.00	2.97	2.99	0.001	0.001	0.002
Cu−C (d) (4)	3.16	3.18	3.15	0.009	0.004	0.003
Cu−C (e) (4)	3.31	3.24	3.25	0.001	0.001	0.001

[a]S_0^2 = 1.0, ΔE= 3.0 eV. [b]Coordination number in parentheses. [c]± 0.02 Å. [d]Debye−Weller factor or σ^2.

Cu−C−C multiple scattering paths are excluded from the Table 4 but were included in the fitting). Both the excited and charge-transfer state spectra reveal a decrease in the average Cu−N bond distance.[38] The average Debye−Waller (DW) factor for the Cu−N paths in the excited-state spectra is smaller than that observed for the ground-state, indicating that the four Cu−N bonds are more equidistant in the excited state than in the ground state, consistent with **2** crystal structures.[62] There are slight changes in the Cu−C(c) and Cu−C(e) distances, which are consistent with the results of the average Cu−N shrinking. However, the Cu−C(d) distances for this complex are nearly identical in the ground state and the excited state. In this case, the Cu−C(d) distances of **3** and **4** as well as **3-TiO$_2$** and **4-TiO$_2$** are similar to that for the excited state of **2**, indicating that little to no further flattening occurs in the excited state.

Another key difference between **4** and **2** is the DW factor for the Cu−C(b) scattering path in the excited state. This DW factor of the latter was extremely high for the photoexcited state but much smaller for the fully oxidized Cu(II) complex; this result was attributed to localization of the electron in the MLCT state onto only one of the ligands, desymmetrizing the structure, including the Cu−C(b) distances, etc. However, if the electron

injection occurs in the hybrids, the electron on the radical phen anion formed from the MLCT transition would be transferred to the TiO_2, and the ligand becomes neutral and the structure, symmetric again. Hence, the electron relay in the MLCT state from the copper center to phen and then to TiO_2 will result in a Cu(II) center and neutral ligands. Such an observed result is indicative of a large degree of electron transfer into TiO_2, which would deplete the radical phen anion and thus mitigate the structural deformations on the phen ligand.

3.6. Computational Results. *3.6.1. Ground-State and ^{3}MLCT Structures.* Initial optimizations were performed on **2**, the parent complex. Three stable conformations of **2** were found, differing by relative orientations of their phenyl moieties at the 2,9-positions. The lowest energy conformer (denoted **2a**, see Figure 9), which is the most flattened of the three, has phenyl
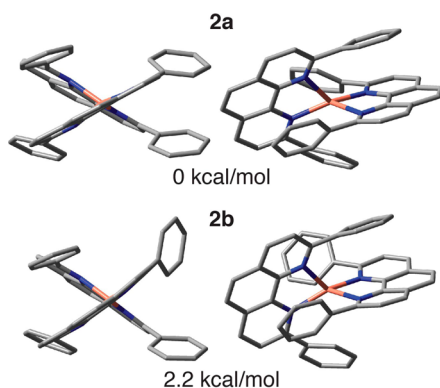

Figure 9. Two lowest energy conformations of **2** optimized at the B3LYP/6-31G*,SDD level of theory in vacuum: (a) both sets of phenyl groups parallel and (b) one set of phenyl groups parallel.

groups that are approximately parallel on either of the two phen ligands. The **2b** conformer with only one set of phenanthroline phenyl groups parallel most closely resembles the crystal structure[62] and is only 2.2 kcal/mol higher than **2a** in energy (see Figure 9). The third structure, **2c**, has an energy 5.6 kcal/mol higher than **2a** and contains no parallel phenyl groups on either ligand (see Figure S11 in SI). The B3LYP SDD/6-31G* optimized structure of **2b** is in good agreement with the crystal structure[62] as the average percent error is 1.9% for the metal–ligand bond lengths and 2.5% for the ligand bite angles.

Conformers analogous to **2** were found for the model complexes **3′** and **4′** and are labeled as **3′a**, **3′b**, **3′c**, **4′a**, **4′b**, and **4′c**. These conformations have the same energetic ordering as conformers of **2** (i.e., $E(a) < E(b) < E(c)$). Metal–ligand bond lengths in the crystal structure of **2** and in the constructed **2a**, **2b**, **3′a**, and **4′a** complexes are not significantly different, suggesting that our chosen computational methodology provides reliable structures for the **3′** and **4′** complexes as well (see Table S3 in SI). All subsequent calculations were performed for the two most stable conformations (**a** and **b**). The results for **2a**, **3′a**, and **4′a** are presented here, while those for **2b**, **3′b**, and **4′b** can be found in the SI. The results for both conformations of **3′** and **4′** lead to the same conclusions regarding the sensitization capabilities of **3** and **4**. In reality, the barrier to convert between the various stable conformations is likely to be quite small[108] (on the same order of magnitude as *kT*), and all conformations could potentially coexist in solution.

For the ^{3}MLCT optimizations of **3′** and **4′**, natural orbital analysis[109] was performed to characterize the excited states. The

SONOs for the two lowest energy ^{3}MLCT states of **3′a** and **4′a** are shown in Figure 10. The two ^{3}MLCT states are almost
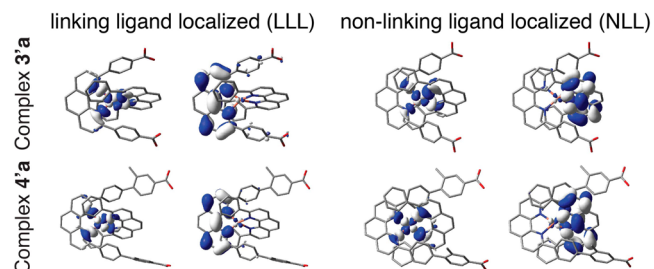

Figure 10. SONOs that characterize ^{3}MLCT states of complexes **3′a** and **4′a**. Two distinct ^{3}MLCT states were obtained for both complexes, one in which the electron localizes on the phenanthroline of the linking ligand (LLL) and one in which electron localizes on the phenanthroline of the nonlinking ligand (NLL) (isovalue = 0.03 e/Å^3).

isoenergetic (differing by 1.2 kcal/mol for **3′a**, 1.4 kcal/mol for **3′b**, 0.3 kcal/mol for **4′a**, and 1.4 kcal/mol for **4′b**), and the ligand-centered SONOs are primarily localized on the phenanthroline π^* system of a single ligand (Figure 10). The results for the optimized ^{3}MLCT states of **3′b** and **4′b** can be found in SI.

3.6.2. Calculated UV–vis Spectra. The calculated UV–vis spectra for **1**, **2a**, and the model complexes **3′a** and **4′a** are shown in Figure 11. The significant excitations in the lower energy
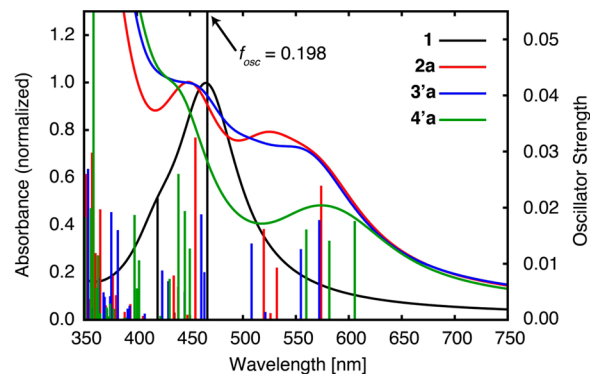

Figure 11. Simulated absorption spectra for complexes **1** (black), **2a** (red), **3′a** (blue), and **4′a** (green). Spectra were calculated at the B3LYP+D/SDD,6-31G* level of theory in methanol (PCM). Lorentzian broadening of hwhm = 0.2 eV was used.

portion of the visible region of their spectra ($\lambda > 400$ nm) are classified as ^{1}MLCT excitations, and those in the higher energy region (350 nm $< \lambda <$ 400 nm) are a combination of ^{1}MLCT and $\pi-\pi^*$ excitations. These excitations form a single broad absorption band for each of the complexes. The TD-DFT calculated spectra are in a reasonable agreement with the experimental spectra (Figure 2) and reproduce the increase in the intensity of the lowest energy MLCT excitation ($S_0 \rightarrow S_1$) as well as the red-shift going from **3** to **4**, due to the flattening of the pseudotetrahedral structure.

The excitations of the model complex **4′a** create several particle states composed of LUMO−LUMO+4 and LUMO+7 KS orbitals shown in Figure 12. These particle states can potentially undergo IET and therefore serve as the initial (or donor) states for the IET simulations utilizing the **4′a**-TiO_2 assemblies.
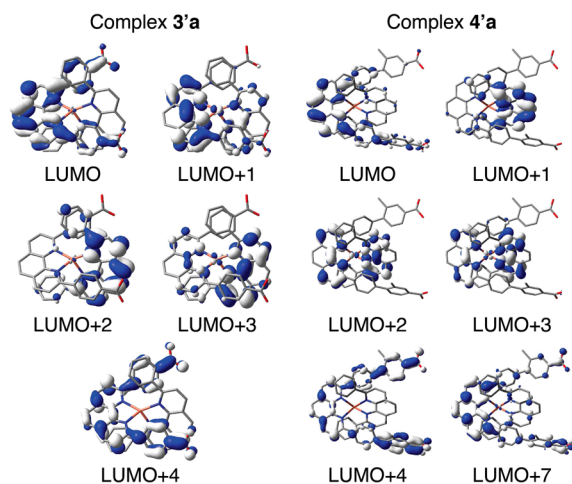
Complex **3'a**   Complex **4'a**

Figure 12. Unoccupied KS orbitals in MeOH (PCM) involved in visible light excitations with $f_{osc} > 0.0075$ for complex **3'a** and **4'a** as determined based on the TD-DFT calculations (isovalue = 0.03 e/Å³).

3.6.3. IET Simulations.

Figure 13 shows the two different binding arrangements investigated for **4'a**-TiO₂ assemblies:
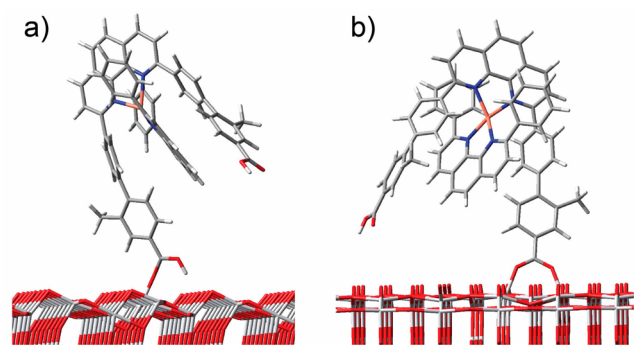

Figure 13. Monodentate (a) and bidentate (b) binding schemes for **4'a** on TiO₂.

monodentate, where the complex binds through one oxygen of a single −COOH group, and bidentate, where the complex binds through two oxygens of a single −COOH group. These two modes were chosen based on previously published stability analysis.[110−114] Attachment through both carboxylate groups was found to be too computationally demanding to investigate (as it would involve structure optimization of the entire chromophore on the TiO₂ surface) and hence is not calculated here. Alignments were performed to consider the feasibility of binding to TiO₂ through both arms, and example structures are shown in Figure S35 of SI. It is unlikely that **3'** is able to bind through both arms due to the steric constraints of the nonlinked ligand group. In the case of **4'**, binding through both arms appears to be plausible but difficult to model with our chosen methodology.

A similar situation exists for modeling the attachment between the **3'** and **4'** structures of the ³MLCT states on TiO₂, with six attachment models for the **3'** ³MLCT states and eight attachment models for each of the ³MLCT states. This leads us to consider a total of 12 **3'**-TiO₂ assemblies and 16 **4'**-TiO₂ assemblies for the ³MLCT states of **4'**. As with the ¹MLCT IET simulations, the **4'a** results are presented for each linker group as an average over the two possible linkers, except in the case of **3'a**

in which only one linker produced physically reasonable models for attachment (all results can be found in the SI).

Density of states (DOS) for the model **4'a**-TiO₂ hybrid in the monodentate attachment mode obtained at the eH level of theory is shown in Figure 14. The DOSs for all other **4'**-TiO₂
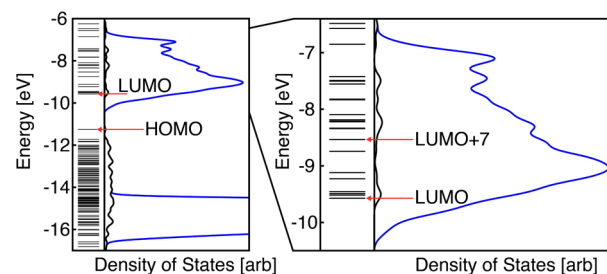

Figure 14. DOS for the monodentate binding mode of **4'a**-TiO₂ anatase (101) slab model (left) and enlarged view of conduction band region (right), calculated by the extended Hückel theory. The plots show the total DOS (blue line), the projected DOS of the adsorbate (black line), and the discrete energy levels of the adsorbate (level set lines).

attachments are virtually identical, and those for the **3'**-TiO₂ systems are not significantly different (example in SI, Figure S36). As can be seen in Figure 14, relevant particle states (or donor states for the IET process) are well within the conduction band region of anatase. Interestingly, LUMO−LUMO+4 orbitals occupy a region where the density of the TiO₂ acceptor states is increasing most rapidly and LUMO+7 is also found in a region with a large density of TiO₂ states (comparable with LUMO+4). The energetic match between the donor states of the dye and the acceptor states of the TiO₂ semiconductor is one of the requirements for efficient IET in dye-semiconductor systems,[92,93,97] therefore these results are promising for utilizing **4'** as a photosensitizer. The **3'** complex also shows promise as a photosensitizer based on the energetic location of the LUMO−LUMO+4 orbitals relative to the conduction band DOS (SI, Figure S30), which is not significantly different from **4'**.

In addition to the energetic alignment of the donor states with the conduction band of the TiO₂, the orbital overlap between the two is also important for facilitating the IET. Since the **3'** and **4'** complexes are attached to TiO₂ via aryl acid groups, the amount of electron density on these groups for a particular donor state is one of the indicators for its spatial localization near the semiconductor surface. Table 5 summarizes the electron density fractions on the aryl acid groups for **3'a** and **4'a** obtained from the Mulliken population analysis performed for each donor state. This was calculated for both the ¹MLCT (LUMO−LUMO+4 for **3'**, and LUMO−LUMO+4 and LUMO+7 for **4'**) as well as ³MLCT (SONOs) donor states. The percent electron density on the benzoic acid linking group in complex **3'a** is small for LUMO+1 and LUMO+3 (<2%) while is relatively large for LUMO, LUMO+2, and LUMO+4 (6−36%). Both of the ³MLCT donor states of **3'a** have a significant amount of electron density on the linker groups (5.3 and 6.5%). The percent of electron density on the toluic acid linking groups of complex **4'a** is small for LUMO+1, LUMO+2, and LUMO+3 donor states (<2.2%) while significantly larger for LUMO, LUMO+4, and LUMO+7 (5−33%). The ³MLCT donor states for this complex have a comparatively small amount of electron density on the linker (≤1.0%), as they are primarily localized on the phen groups.

The calculated characteristic IET times for all donor states investigated are also shown in Table 5, ranging from 6.8 fs to 3.0

Table 5. Percent Electron Density on Aryl-Carboxylic Acid Group and Calculated Characteristic IET Times for 3′a-TiO$_2$ and 4′a-TiO$_2$

	complex 3′a			complex 4′a		
		characteristic IET time			characteristic IET time[c]	
donor states[a]	avg. density [%]	monodenate	bidentate	avg. density[b] [%]	monodentate	bidentate
LUMO	16.9	148.7 fs	123.8 fs	5.0	262.5 fs	169.9 fs
LUMO+1	0.6	3.0 ps	487.2 fs	1.9	1.2 ps	149.0 fs
LUMO+2	6.2	579.9 fs	216.0 fs	1.8	371.2 fs	119.4 fs
LUMO+3	1.5	2.1 ps	1.1 ps	2.1	281.4 fs	77.5 fs
LUMO+4	36.0	9.0 fs	6.8 fs	33.0	14.7 fs	12.1 fs
LUMO+7	–	–	–	11.3	118.3 fs	57.4 fs
SONO−LLL[c]	5.3	1.2 ps	92.0 fs	1.0	1.6 ps	401.6 fs
SONO−NLL[c]	6.5	945.4 fs	79.3 fs	0.1	>20 ps	>20 ps

[a]LUMO−LUMO+4 and LUMO+7 denote donor states for IET from ^{1}MLCT states, while SONO−LLL, and SONO−NLL label donor states from ^{3}MLCT initial states (LLL is linking ligand localized state, NLL is nonlinking ligand localized state). [b]% Electron density is averaged over the two toluic acid groups, obtained from eH calculations. [c]Characteristic IET times are given as an average of the IET times calculated for attachment via either toluic acid linker.

ps for 3′a-TiO$_2$ and 12 fs to 1.2 ps for 4′a-TiO$_2$ when the IET occurs from the ^{1}MLCT-state manifolds. These results are consistent with the <300 fs time constant obtained from the ultrafast TA measurements. These characteristic IET time constants are also shorter than those for the Jahn−Teller flattening time and ISC, agreeing with the experimental finding that the majority of electron injection occurs from the initially populated higher energy ^{1}MLCT complex. The evidence for strong coupling between the donor excited states with the TiO$_2$ acceptor states is (1) fast IET rates, (2) the donor excited-state energetic position well into the conduction band of the TiO$_2$ acceptor with large DOS, and (3) spatial delocalization over the toluic acid linking group. Based on these results, differences in characteristic IET time constants from ^{1}MLCT excited states of 3′ and 4′ are insignificant.

We can further compare the sensitization capabilities of the ^{1}MLCT states of 3′ and 4′ by calculating the expectation value for the injection time at the excitation wavelengths, which are shown in Figure 15. The IET times for 3′-TiO$_2$ from the ^{1}MLCT states are generally slower than in 4′-TiO$_2$ but not drastically different. Both complexes have excitations that lead to rapid IET (<100 fs) in the higher energy region (<500 nm) of the spectrum. The averages over the entire range of calculated expectation values for IET times shown in Figure 15 are 968.7 fs for 3′a and 287.3 fs for 4′a.

The ^{3}MLCT states of complex 3′ are significantly delocalized over the linker group, whereas those of 4′ are primarily localized on the phen ligands and have only a small amount of electron density on the linker group. Consequently, the IET times from the ^{3}MLCT states of 3′ are relatively fast (from 79.3 fs to 1.2 ps) compared to those of 4′ (from 400 fs to > 20 ps). Visualization of the wave packets evolution as a function at each time step of the quantum dynamics simulations reveals that the IET proceeds for 3′ through a rapid dumping of electron density into the surface both through the linker and potentially through space and for 4′ via a slow drain of the electron density from the phenanthroline π system through the π system of the linker arm and into the TiO$_2$ surface. The IET from the ^{3}MLCT states localized on the linking ligand is more efficient than the IET from the nonlinking ligand localized states by at least an order of magnitude for 4′ (see Table 5) but is not significantly different for 3′, which for 3′a is likely a result of the states being overly delocalized. This can be explained by the differences in the percent of electron density on the linking
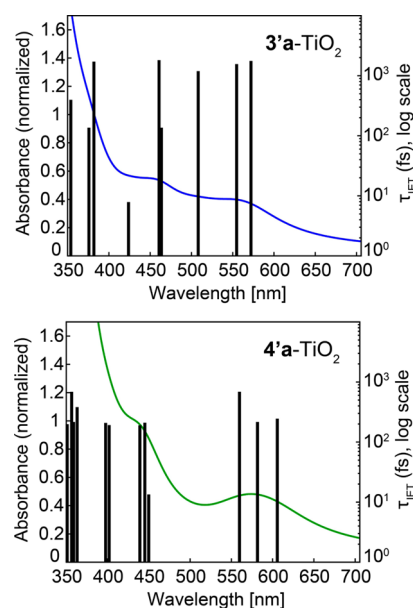

Figure 15. Characteristic IET times (τ_{IET}, bars) calculated for linear combinations of singlet excited states (TD-DFT) overlaid on simulated spectra (lines) of chromophores for 3′a-TiO$_2$ (top) and 4′a-TiO$_2$ (bottom).

toluic acid group between the two ^{3}MLCT states for 4′ (2.0% vs 0.2%, see Table 5), while 3′ has significant density on the linker for both states.

It is worth noting that the two lowest energy ^{3}MLCT states of 3′ and of 4′ are both approximately degenerate pairs. Therefore, they will very likely be coupled through vibrational motion, so that an excited electron could undergo interligand electron transfer between the two ligands on a subpicosecond time scale.[115] Such a mechanism could potentially enable IET even from the ^{3}MLCT state initially localized on the nonlinking phenanthroline ligand of 3′ and 4′.

Finally, the characteristic times for the IET originating from the ^{3}MLCT states populating the nonlinking ligand of 4′ (401.6 fs and 1.6 ps) are several orders of magnitude shorter than the lifetime of the ^{3}MLCT excited state (150 ns). Therefore, the IET from the longer-lived ^{3}MLCT states is a feasible mechanism for the TiO$_2$ sensitization by complex 4′.

4. DISCUSSION

4.1. Structural Factors in Excited State Influencing Interfacial Charge Transfer.
As mentioned in the introduction, some concerns have been raised about the use of Cu(I) diimine complexes for solar energy conversion in place of their Ru(II) counterparts. The synthetic designs of **3** and **4** were aimed at achieving: (1) a long-lived ^{3}MLCT state to allow for efficient electron injection into TiO$_2$, (2) a higher driving force for efficient IET from the initially excited ^{1}MLCT state, (3) the ligation stability of the Cu(II) moiety in the excited state, and (4) stable binding of Cu(I) complexes to TiO$_2$ nanoparticles. So far, our results have proven that these requirements have been met successfully. The attachment of phenyl groups at 2,9 positions of the diimine ligand simultaneously blocks the solvent access to the Cu(II) center in the MLCT state and flattens the pseudotetrahedral coordination environment around Cu(I), which consequently lowers the spin−orbit coupling,[57] thus prolonging the ^{1}MLCT-state lifetime and allowing the IET to compete favorably with a higher driving force. The new Cu complexes are also stabilized by the presence of the catenane loop with no evidence of decomposition.

In particular, significant changes in the photophysical properties occur due to the structural distortions in **3** and **4** from the pseudotetrahedral coordination geometry in **1**, such as aforementioned broadened and red-shifted absorption features, which ultimately alter the molecular potential energy landscape, allowing the otherwise symmetry forbidden transitions and broadening the overlap with the solar spectrum as a result of the transition energy splitting. Based on the optical TA spectra and the structures of the ground and excited states determined from EXAFS studies as well as DFT calculations, a potential energy diagram can be constructed for these complexes as shown in Figure 16. In the ground-state absorption spectra of **3** and **4** (Figure 2), the lower energy transition (centered at ~550 nm) corresponds to the S$_1$ ← S$_0$ transition (the green line in Figure 16A) with the MLCT origin, which is only allowed in the flattened geometry. Meanwhile, the higher energy transition designated to the S$_2$ ← S$_0$ transition (the blue line in Figure 16A)

with a combination of the MLCT and $\pi^* \leftarrow \pi$ transitions. It must be clarified that S$_1$ and S$_2$ here are designated generally for all Cu(I) diimine complexes with pseudotetrahedral coordination geometry or otherwise in the ground state. Transitions to both S$_1$ and S$_2$ states are allowed in flattened pseudotetrahedral geometry, while only the transition to the S$_2$ state is allowed in completely locked pseudotetrahedral geometry; in the latter case, S$_2$ will be the lowest energy excited state. The fact that the 600 fs rise time constant was still observable in the TA results of **3** and **4** in solution, respectively, indicates that further structural reorganization in the ^{1}MLCT state along the flattening coordinate takes place as shown by the computed results of an ~10° smaller angle between the two ligand planes as well as energetically coexisting/interconverting conformations (Figure 8). Meanwhile, the flattening distortion also stabilizes the orbitals in the excited state that have weak spin−orbit couplings, giving rise to the prolonged ^{1}MLCT-state lifetime of ~11 ps and enabling the IET to compete favorably with the intersystem crossing. The MLCT-state lifetime in polar solvent is prolonged due to the shielding of the copper center in the MLCT state from direct encounter of the solvent molecules. Hence, aryl-substituted copper bis-phen complexes are ideal for implementation in solar energy conversion devices due to their large spectral coverage, fast IET, and stability in polar solvents.

The FT-EXAFS spectra are also consistent with increased ground-state flattening. It has been shown that, in the ground state for **2**, a phenyl ring rotates to maximize $\pi-\pi$ interactions with the opposing phenanthroline ligand.[62] In the photoexcited state for **2**, the phenanthroline flattening angle changes by ~7°, and the 2,9 substituted phenyl rings lose their $\pi-\pi$ interactions with the phenanthroline ligand and rotate by ~10°, resulting in a smaller Cu−C(d) distance and an increase in the DW factor of the corresponding scattering path.[38] The Cu−C(d) path distance and DW factor for **4**, in the ground and excited states, are both consistent with that measured in the excited state of **2**, indicating that the ground state of **4** is more flattened than that of **2**. Such assessment is also consistent with the further red-shifted and amplitude enhanced shoulder feature for **3** and **4** compared to **2** (Figure 2).

The calculated UV−vis spectra of **2**, **3′**, and **4′** also show a significant increase in the intensity of the lowest energy ^{1}MLCT transition in comparison to the spectrum of **1** (see Figure 11 and Figure S34 in SI). The optimized ground-state structures of these complexes display both $\pi-\pi$ interactions between the phenyl rings and phenanthroline ligands as well as flattening the two ligand planes to ~70° in case of the lowest energy conformers or to ~80° in case of the higher energy conformers (see Table S4 in SI). Moreover, the lowest energy ^{1}MLCT transitions are the most intense for conformers displaying the largest amount of flattening (see Figure S34 in the SI). Although the calculations do not show significant changes in the phenanthroline-phenyl dihedral angle between the ground state and ^{3}MLCT state (see Tables S4 and S5 in the SI), the optimized ^{3}MLCT excited states for **2**, **3′**, and **4′** display additional flattening by 7−10° respected to their ground-state structures (see Table S5 in the SI), which is consistent with the experimental results.

4.2. Influence of TiO$_2$ Binding on Molecular Structures of the Ground and Excited States.
In order to simulate the IET process in the hybrids of **3**-TiO$_2$ and **4**-TiO$_2$, it is important to determine the effect on the structure of **3** and **4** upon binding TiO$_2$ in these DSSC mimics. As we have learned from above, structural changes in Cu(I) diimine complexes, although sometimes rather minor, could affect both dynamics and
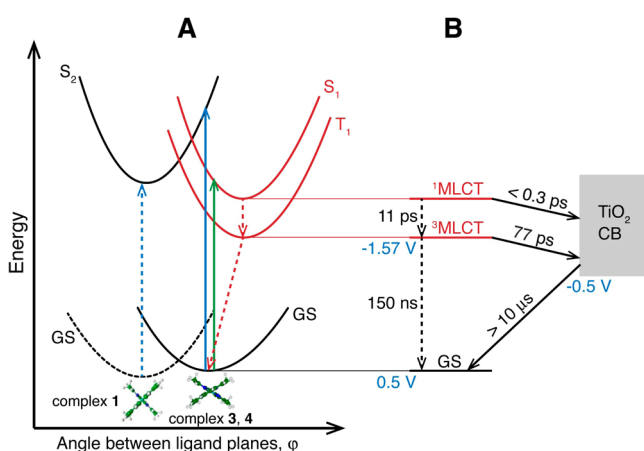

Figure 16. (A) A general description of potential energy surfaces associated with the angle between the two phen ligands in Cu(I) diimine complexes; in flattened pseudotetrahedral conformation as in **3** and **4**, the blue and green lights induce the S$_0$ → S$_2$ and S$_0$ → S$_1$ transitions, respectively; and S$_1$ and T$_1$ correspond to ^{1}MLCT and ^{3}MLCT respectively as shown in (B), energy levels (blue) and time constants (black) for the IET process in **3**- and **4**-TiO$_2$. The vibrational manifolds are omitted for simplicity.

energetics of their MLCT states as well as the IET efficiency. As shown in Table 3, no significant structural changes in the ground states of **4** and **4**-TiO$_2$ within the experimental errors. Since the scattering path distance and DW factor for the Cu—C(d) path are the same both in solution and on TiO$_2$, implying that the optimal rotation angle for the phenyl rings can be retained upon binding to TiO$_2$. Such structural invariance suggests fits the expectation that most of the binding is mostly through one instead two linkers at 2 or 9 positions resulting minimal structural constraints upon binding to TiO$_2$ nanoparticles.

Based on our previous studies of several Cu(I) diimine complexes,[32,38,39,41,42,67] the MLCT states of these complexes are associated with significant structural reorganizations, in particular the large decrease in the angle between the two ligand planes. Such structural changes affect the excited-state energy of these complexes and therefore should influence both the electron transfer and charge recombination rates in these systems. In this case, the structural dynamics of **3** and **4**, with the exception of the phenyl ring rotation, are comparable to those of **2**. Furthermore, there is little to no difference between the structures of these complexes in the photoexcited state or in the charge transfer state, indicating that the phenyl ring rotation is likely not a crucial step in the electron- transfer process.

4.3. Mechanism of the IET. Based on our combined experimental and computational studies, two mechanisms for the IET in **3**-TiO$_2$ and **4**-TiO$_2$ assemblies can be proposed: (1) A hopping mechanism, in which the electron transfers directly from the phenanthroline ligand into the TiO$_2$ surface; and (2) a through-bond mechanism, where the electronic wavepacket travels across the linking arm and enters TiO$_2$ nanoparticle via the carboxylic acid anchoring group. In this section, we will discuss the experimental and computational evidence for these two mechanisms.

4.3.1. Hopping Mechanism. ET in donor−acceptor assemblies is usually distance dependent, meaning that a longer linker group should result in a slower rate of the electron transfer from the excited dye into the semiconductor.[116] Based on these considerations one would expect the IET in **4**-TiO$_2$ assemblies to be less efficient than in **3**-TiO$_2$ assemblies, due to the presence of an additional phenyl group in the linker that anchors **4** to the TiO$_2$ surface. Contrary to these expectations, the IET in both assemblies occurs on the same rate, which points toward a possible hopping mechanism of the IET.

A similar IET process was observed in TiO$_2$ sensitized with a Zn porphyrin,[117] which connected to the nanoparticle via two phenyl rings and a carboxylate group. IET was determined to occur via hopping directly from the porphyrin ring into the TiO$_2$, not through the phenyl chains. Such an arrangement resulted in IET that is dependent upon the tilt angle between the sensitizer and TiO$_2$ and charge recombination on the tens to hundreds of picoseconds time scale, which would be consistent with the 6.0 ps decay time measured in the TA data here.[117]

Computationally, we do not observe evidence for hopping mechanism. It is, however, possible that inclusion of additional features into the quantum dynamics simulation, such as taking into consideration additional binding modes (e.g., through both linkers simultaneously) or inclusion of nuclear dynamics, might activate the hopping pathway. Therefore, we cannot exclude hopping as the mechanism of IET in Cu(I) dye-TiO$_2$ assemblies at this time.

4.3.2. Through-Bond Mechanism. Analysis of the results of our IET simulations in the **3′**-TiO$_2$ and **4′**-TiO$_2$ assemblies points to the through-bond mechanism, as the electronic

wavepacket travels into the TiO$_2$ surface predominantly via the carboxylic acid anchoring groups. Moreover, our simulations reproduce the experimentally measured fast IET in **4**-TiO$_2$ assemblies (see Table 5 and Figure 15), suggesting that a fast IET transfer occurs in **4′**-TiO$_2$ despite the lengthened linker group. The fast through-bond IET can be explained by examining the MOs populated upon the visible excitation of complex **4′** (see Figure 12). Several of the MOs display significant electron density on the anchoring group. Previous studies of Fe(II)-polypyridine-TiO$_2$ assemblies by Jakubikova and co-workers have shown that the presence of electron density on the anchor group is one of the main factors that controls the speed of the IET in dye-sensitized TiO$_2$.[92,93,97,118] Several of the ^{3}MLCT states of complex **4′** display nonzero electron density on the linker group as well (0.3−0.7% on average, see Table S22 in SI), suggesting that the through-bond mechanism can play a role for IET originating from these states as well. These states are, however, almost fully localized on the phenanthroline ligands, which is reflected in the slower calculated characteristic IET times in comparison to **3′**-TiO$_2$ assemblies (see Table 5).

Overall, we conclude that the IET in **3**-TiO$_2$ and **4**-TiO$_2$ assemblies occur via the through-bond mechanism, especially for the IET originating from the initially excited ^{1}MLCT states. It is possible that the hopping mechanism also plays a role in these systems, and if present, it would be more important for the IET originating from the longer-lived ^{3}MLCT states.

4.4. Structural Influences on IET Pathways. Previous computational investigation of the lowest energy conformation of **2** has determined that conjugation between the phenyls and the phenanthroline ligands is poor in the ^{3}MLCT states.[38] Our DFT calculations for complexes **3′** and **4′**, which are derived from **2**, are consistent with these conclusions and show that the ^{3}MLCT states are primarily localized on the phenanthroline ligand (see Figure 11 and Figures S20 and S29 in SI). However, several of the ^{3}MLCT states obtained for complexes **3′** display some degree of delocalization onto the linker groups, with 1−9% electron density (see Table S22 in SI). Hence while the phenyl-phenanthroline conjugation is mostly poor for these systems, it is not nonexistent, and the lifetime of the ^{3}MLCT states is likely adequate to allow for the IET in **3**-TiO$_2$ and **4**-TiO$_2$ assemblies.

One way to improve the IET rate in these systems would be to increase the electron density on the linker group and build energy cascade for the MLCT orbitals in favor of the electron-transfer direction. Such systems could be achieved by substituting the carboxylic acid group at 4,7 or 5,6 positions of the phenanthroline moiety in **2** complex while keeping the catenane loop to stabilize Cu(II) species. Similar to the RuN3 dye in DSSC, the energy cascade from the Ru−NCS moiety to Ru-bcbpy [bis(4,4′-dicarboxy-2,2′-bipyridine] moiety that directly linked to TiO$_2$, the same kind of energy cascade needs to be constructed to ensure effective injection. Our preliminary calculations indicate that both of these aforementioned substitutions delocalize the ligand-based SONO of the ^{3}MLCT state over the linker (see Figure S37 in the SI). An added benefit of these substitutions is that the degeneracy of the two lowest energy ^{3}MLCT states, observed in **3′** and **4′**, is broken and linker-localized state becomes the lowest in energy. This means that the low-lying ^{1}MLCT states or the long-lived ^{3}MLCT state will have an excellent potential for coupling with the TiO$_2$ acceptor states.

A drawback of **3**-TiO$_2$ and **4**-TiO$_2$ assemblies is that while they do exhibit a very fast IET, they could also experience fast charge recombination, limiting their usefulness in DSSCs. Electron recombination could potentially be minimized by modulating the

relative energy levels of the orbitals involved in IET from high to low, so that the TiO_2 will act like a trap for the electrons. In the current design of **3**-TiO_2 and **4**-TiO_2 assemblies, the MLCT and IET directions via the linkers are not aligned, which may be in part the reason for relatively fast charge recombination. A ligand and linker system like $[Cu(I)(dppS)_2]^+$ appears to be an efficient IET system which merely "sticks" to the TiO_2 surface via electrostatic interactions of the $-SO_3$ groups. This complex displays efficient IET and slow recombination despite the fact that the MLCT states localized on two dppS ligands are equivalent and there is no preferential electron localization on the dppS ligand closer to the TiO_2 surface. We hypothesize that because $[Cu(I)(dppS)_2]^+$ may not bind to TiO_2 via covalent bonds, it is possible for the dye to reorient itself relative to the TiO_2 surface both before and after the IET and thus achieve both fast IET and minimize recombination. TA anisotropy measurements showed that **1** tumbles in solution with a time constant of 31 ps.[36] This time constant is on a similar scale to singlet-state charge recombination and is likely much shorter than the recombination time for the triplet state, indicating that tumbling in solution could indeed effect charge recombination. Furthermore, on longer time scales the copper system can diffuse away from the TiO_2 surface, which would further limit interactions with the TiO_2 following ET. The proposed methods for preventing charge recombination are necessary if such a system is to be implemented into DSSCs, as charge recombination must be inhibited so that the copper center can be reduced by the redox couple.

5. CONCLUSIONS

The electronic and structural properties of **3** and **4** were successfully synthesized to facilitate photophysical properties and chemical stability that enable these complexes to perform efficient IET in their hybrid with TiO_2 nanoparticles, mimicking DSSCs. These systems were investigated with experimental and computational methods employing optical and X-ray transient spectroscopies as well as DFT and TD-DFT calculations. Applying structural constraints due to the aromatic groups in the 2,9-positions to force flattened coordination geometry, these complexes exhibited broadened optical absorption to enhance the overlap with the solar spectrum, prolonged the singlet and triplet MLCT excited-state lifetimes, and enabled large fractions of the ^{1}MLCT state to perform IET on the subpicosecond time scale with a long lasting charge-separated state up to several microseconds. The results from DFT and TD-DFT calculations as well as quantum dynamics simulations agreed well with the experimental results on spectroscopic features and excited-state structures as well as the IET dynamics. More importantly, we determined that both a through-bond and a chromophore to surface hopping mechanisms are plausible for IET in **3**- and **4**-TiO_2 assemblies. While these complexes showed potential as sensitizers for TiO_2, considerations must be made to the structural design based on the through-bond IET mechanism, so as to design a molecule with an ideal alignment to the semiconductor surface that would enhance preferentially efficient IET but inhibit the charge recombination. We propose two different pathways for further improvement of complex **3** and **4**. These include substitution of the carboxylic acid anchoring group at 4 or 5 position of the phenanthroline group or use of the sulfonate group in place of the carboxylic acid linker. Such a system could serve as a cheaper alternative to expensive ruthenium dyes for solar energy conversion devices.

■ ASSOCIATED CONTENT

ⓈSupporting Information

Nanosecond TA of **3** in methanol and on TiO_2; synthetic procedures for **3** and **4**; NMR spectra for **3** and **4**; CIF file for **4**; TA and XAFS spectra of **3** in methanol and on TiO_2; calculated structural parameters, TD-DFT analysis, SONOs, IET results, and density on linker groups for **3′** and **4′**. The Supporting Information is available free of charge on the ACS Publications website at DOI: 10.1021/jacs.5b04612.

■ AUTHOR INFORMATION

Corresponding Authors
*lchen@anl.gov or l-chen@northwestern.edu
*ejakubi@ncsu.edu
*coskun@kaist.ac.kr

Author Contributions
#These authors contributed equally.

Notes
The authors declare no competing financial interest.

■ ACKNOWLEDGMENTS

■ REFERENCES

(1) Nazeeruddin, M. K.; Grätzel, M. *Structure and Bonding*; Springer-Verlag: Berlin, 2007; Vol *123*, pp 113−175.

(2) Grätzel, M. J. *J. Photochem. Photobiol., C* **2003**, *4*, 145−153.

(3) McCusker, J. K. *Acc. Chem. Res.* **2003**, *36*, 876−887.

(4) Paris, J. P.; Brandt, W. W. J. *J. Am. Chem. Soc.* **1959**, *81*, 5001−5002.

(5) Juris, A.; Balzani, V.; Barigelletti, F.; Campagna, S.; Belser, P.; von Zelewsky, A. *Coord. Chem. Rev.* **1988**, *84*, 85−277.

(6) Damrauer, N. H.; Cerullo, G.; Yeh, A.; Boussie, T. R.; Shank, C. V.; McCusker, J. K. *Science* **1997**, *275*, 54−57.

(7) Verma, S.; Kar, P.; Das, A.; Ghosh, H. N. *Chem. - Eur. J.* **2011**, *17*, 1561−1568.

(8) Kuciauskas, D.; Monat, J. E.; Villahermosa, R.; Gray, H. B.; Lewis, N. S.; McCusker, J. K. *J. Phys. Chem. B* **2002**, *106*, 9347−9358.

(9) Ardo, S.; Sun, Y.; Castellano, F. N.; Meyer, G. J. *J. Phys. Chem. B* **2010**, *114*, 14596−14604.

(10) Ma, D.; Bettis, S. E.; Hanson, K.; Minakova, M.; Alibabaei, L.; Fondrie, W.; Ryan, D. M.; Papoian, G. A.; Meyer, T. J.; Waters, M. L.; Papanikolas, J. M. *J. Am. Chem. Soc.* **2013**, *135*, 5250–5253.

(11) Zou, L.-Y.; Ma, M.-S.; Zhang, Z.-L.; Li, H.; Cheng, Y.-X.; Ren, A.-M. *Org. Electron.* **2012**, *13*, 2627–2638.

(12) Lemus, L.; Ferraudi, G.; Lappin, A. G. *Dalton Trans.* **2013**, *42*, 8637–8643.

(13) Lazorski, M. S.; Gest, R. H.; Elliott, C. M. *J. Am. Chem. Soc.* **2012**, *134*, 17466–17469.

(14) McMillin, D. R.; Kirchhoff, J. R.; Goodwin, K. V. *Coord. Chem. Rev.* **1985**, *64*, 83–92.

(15) Ruthkosky, M.; Kelly, C. A.; Castellano, F. N.; Meyer, G. J. *Coord. Chem. Rev.* **1998**, *171*, 309–322.

(16) Ruthkosky, M.; Castellano, F. N.; Meyer, G. J. *Inorg. Chem.* **1996**, *35*, 6406–6412.

(17) Lavie-Combot, A.; Cantuel, M.; Leydet, Y.; Jonusauskas, G.; Bassani, D. M.; McClenaghan, N. D. *Coord. Chem. Rev.* **2008**, *252*, 2572–2584.

(18) Gray, H. B.; Maverick, A. W. *Science* **1981**, *214*, 1201–1205.

(19) Smith, C. S.; Mann, K. R. *Chem. Mater.* **2009**, *21*, 5042–5049.

(20) Bessho, T.; Constable, E. C.; Graetzel, M.; Hernandez Redondo, A.; Housecroft, C. E.; Kylberg, W.; Nazeeruddin, M. K.; Neuburger, M.; Schaffner, S. *Chem. Commun.* **2008**, 3717–3719.

(21) Mutrofin, S.; Chan, E. J.; Healy, P. C.; Marinnelli, A.; Ngoune, J.; Pettinari, C.; Pettinari, R.; Somers, N.; Skelton, B. W.; White, A. H. *Inorg. Chim. Acta* **2008**, *361*, 2365–2374.

(22) Lenzmann, F. O.; Kroon, J. M. *Adv. OptoElectron.* **2007**, *2007*, 1–10.

(23) Armaroli, N.; Accorsi, G.; Cardinali, F.; Listorti, A.; *Topics in Current Chemistry*; Springer-Verlag: Berlin, 2007; Vol *280*, pp 69–115.

(24) Gunaratne, T.; Rodgers, M. A. J.; Felder, D.; Nierengarten, J.-F.; Accorsi, G.; Armaroli, N. *Chem. Commun.* **2003**, 3010–3011.

(25) Armaroli, N. *Chem. Soc. Rev.* **2001**, *30*, 113–124.

(26) Scaltrito, D. V.; Thompson, D. W.; O'Callaghan, J. A.; Meyer, G. J. *Coord. Chem. Rev.* **2000**, *208*, 243–266.

(27) Bozic-Weber, B.; Constable, E. C.; Housecroft, C. E. *Coord. Chem. Rev.* **2013**, *257*, 3089–3106.

(28) Krylova, V. A.; Djurovich, P. I.; Aronson, J. W.; Haiges, R.; Whited, M. T.; Thompson, M. E. *Organometallics* **2012**, *31*, 7983–7993.

(29) Bozic-Weber, B.; Brauchli, S. Y.; Constable, E. C.; Furer, S. O.; Housecroft, C. E.; Malzner, F. J.; Wright, I. A.; Zampese, J. A. *Dalton Trans.* **2013**, *42*, 12293–12308.

(30) Brauchli, S. Y.; Bozic-Weber, B.; Constable, E. C.; Hostettler, N.; Housecroft, C. E.; Zampese, J. A. *RSC Adv.* **2014**, *4*, 34801–34815.

(31) Brauchli, S. Y.; Constable, E. C.; Housecroft, C. E. *Dyes Pigm.* **2015**, *113*, 447–450.

(32) (a) Huang, J.; Buyukcakir, O.; Mara, M. W.; Coskun, A.; Dimitrijevic, N. M.; Barin, G.; Kokhan, O.; Stickrath, A. B.; Ruppert, R.; Tiede, D. M.; Stoddart, J. F.; Sauvage, J. P.; Chen, L. X. *Angew. Chem., Int. Ed.* **2012**, *51*, 12711–12715. (b) Huang, J.; Mara, M. W.; Stickrath, A. B.; Kokhan, O.; Harpham, M. R.; Haldrup, K.; Shelby, M. L.; Zhang, X.; Ruppert, R.; Sauvage, J.-P.; Chen, L. X. *Dalton Trans.* **2014**, *43*, 17615–17623.

(33) Malzner, F. J.; Brauchli, S. Y.; Constable, E. C.; Housecroft, C. E.; Neuburger, M. R. *RSC Adv.* **2014**, *4*, 48712–48723.

(34) Sandroni, M.; Favereau, L.; Planchat, A.; Akdas-Kilig, H.; Szuwarski, N.; Pellegrin, Y.; Blart, E.; Le Bozec, H.; Boujtita, M.; Odobel, F. *J. Mater. Chem. A* **2014**, *2*, 9944–9947.

(35) Sandroni, M.; Kayanuma, M.; Planchat, A.; Szuwarski, N.; Blart, E.; Pellegrin, Y.; Daniel, C.; Boujtita, M.; Odobel, F. *Dalton Trans.* **2013**, *42*, 10818–10827.

(36) Shaw, G. B.; Grant, C. D.; Shirota, H.; Castner, E. W., Jr.; Meyer, G. J.; Chen, L. X. *J. Am. Chem. Soc.* **2007**, *129*, 2147–2160.

(37) Rorabacher, D. B. *Chem. Rev.* **2004**, *104*, 651–698.

(38) (a) Mara, M. W.; Jackson, N. E.; Huang, J.; Stickrath, A. B.; Zhang, X.; Gothard, N. A.; Ratner, M. A.; Chen, L. X. *J. Phys. Chem. B* **2013**, *117*, 1921–1931. (b) Mara, M. W.; Fransted, K. A.; Chen, L. X. *Coord. Chem. Rev.* **2015**, *282-283*, 2–18.

(39) Gothard, N. A.; Mara, M. W.; Huang, J.; Szarko, J. M.; Rolczynski, B.; Lockard, J. V.; Chen, L. X. *J. Phys. Chem. A* **2012**, *116*, 1984–1992.

(40) Huang, J.; Mara, M. W.; Stickrath, A. B.; Kokhan, O.; Harpham, M. R.; Haldrup, K.; Shelby, M. L.; Zhang, X.; Ruppert, R.; Sauvage, J.-P.; Chen, L. X. *Dalton Trans* **2014**, *43*, 17615–17623.

(41) Chen, L. X.; Shaw, G. B.; Novozhilova, I.; Liu, T.; Jennings, G.; Attenkofer, K.; Meyer, G. J.; Coppens, P. *J. Am. Chem. Soc.* **2003**, *125*, 7022–7034.

(42) Chen, L. X.; Jennings, G.; Liu, T.; Gosztola, D. J.; Hessler, J. P.; Scaltrito, D. V.; Meyer, G. J. *J. Am. Chem. Soc.* **2002**, *124*, 10861–10867.

(43) Iwamura, M.; Takeuchi, S.; Tahara, T. *J. Am. Chem. Soc.* **2007**, *129*, 5248–5256.

(44) Penfold, T. J.; Karlsson, S.; Capano, G.; Lima, F. A.; Rittmann, J.; Reinhard, M.; Rittmann-Frank, M. H.; Braem, O.; Baranoff, E.; Abela, R.; Tavernelli, I.; Rothlisberger, U.; Milne, C. J.; Chergui, M. *J. Phys. Chem. A* **2013**, *117*, 4591–4601.

(45) Patterson, G. S.; Holm, R. H. *Bioinorg. Chem.* **1975**, *4*, 257–275.

(46) Kirchhoff, J. R.; Roland, E.; Gamache, J.; Blaskie, M. W.; Del Paggio, A. A.; Legel, R. K.; McMillin, D. R. *Inorg. Chem.* **1983**, *22*, 2380–2384.

(47) Smolentsev, G.; Sukharina, G.; Soldatov, A. V.; Chen, L. X. *Nucl. Instrum. Methods Phys. Res., Sect. A* **2009**, *603*, 122–124.

(48) Smolentsev, G.; Soldatov, A. V.; Chen, L. X. *J. Phys. Chem. A* **2008**, *112*, 5363–5367.

(49) Scaltrito, D. V.; Thompson, D. W.; O'Callaghan, J. A.; Meyer, G. J. *Coord. Chem. Rev.* **2000**, *208*, 243–266.

(50) Bush, P. M.; Whitehead, J. P.; Pink, C. C.; Gramm, E. C.; Eglin, J. L.; Watton, S. P.; Pence, L. E. *Inorg. Chem.* **2001**, *40*, 1871–1877.

(51) Watton, S. *Acta Crystallogr., Sect. E: Struct. Rep. Online* **2010**, *66*, m1449.

(52) Watton, S. *Acta Crystallogr., Sect. E: Struct. Rep. Online* **2009**, *65*, m585–m586.

(53) Lockard, J. V.; Kabehie, S.; Zink, J. I.; Smolentsev, G.; Soldatov, A.; Chen, L. X. *J. Phys. Chem. B* **2010**, *114*, 14521–14527.

(54) McCusker, C. E.; Castellano, F. N. *Inorg. Chem.* **2013**, *52*, 8114–8120.

(55) Miller, M. T.; Karpishin, T. B. *Inorg. Chem.* **1999**, *38*, 5246–5249.

(56) Blaskie, M. W.; McMillin, D. R. *Inorg. Chem.* **1980**, *19*, 3519–3522.

(57) Siddique, Z. A.; Yamamoto, Y.; Ohno, T.; Nozaki, K. *Inorg. Chem.* **2003**, *42*, 6366–6378.

(58) Iwamura, M.; Watanabe, H.; Ishii, K.; Takeuchi, S.; Tahara, T. *J. Am. Chem. Soc.* **2011**, *133*, 7728–7736.

(59) Zgierski, M. Z. *J. Chem. Phys.* **2003**, *118*, 4045–4051.

(60) Meyer, M.; Albrecht-Gary, A.-M.; Dietrich-Buchecker, C. O.; Sauvage, J.-P. *Inorg. Chem.* **1999**, *38*, 2279–2287.

(61) Samia, A. C. S.; Cody, J.; Fahrni, C. J.; Burda, C. *J. Phys. Chem. B* **2004**, *108*, 563–569.

(62) Miller, M. T.; Gantzel, P. K.; Karpishin, T. B. *Inorg. Chem.* **1998**, *37*, 2285–2290.

(63) Chen, L. X. *Annu. Rev. Phys. Chem.* **2005**, *56*, 221–254.

(64) Chen, L. X. *J. Electron Spectrosc. Relat. Phenom.* **2001**, *119*, 161–174.

(65) Harpham, M. R.; Nguyen, S. C.; Hou, Z.; Grossman, J. C.; Harris, C. B.; Mara, M. W.; Stickrath, A. B.; Kanai, Y.; Kolpak, A. M.; Lee, D.; Liu, D.-J.; Lomont, J. P.; Moth-Poulsen, K.; Vinokurov, N.; Chen, L. X.; Vollhardt, K. P. C. *Angew. Chem., Int. Ed.* **2012**, *51*, 7692–7696.

(66) Chen, L. X.; Zhang, X. *J. Phys. Chem. Lett.* **2013**, *4*, 4000–4013.

(67) Chen, L. X.; Zhang, X.; Shelby, M. L. *Chem. Sci.* **2014**, *5*, 4136–4152.

(68) Becke, A. D. *J. Chem. Phys.* **1993**, *98*, 5648–5652.

(69) Stephens, P.; Devlin, F.; Chabalowski, C. F.; Frisch, M. J. *J. Phys. Chem.* **1994**, *98*, 11623–11627.

(70) Grimme, S. J. *J. Comput. Chem.* **2006**, *27*, 1787–1799.

(71) Kaupp, M.; Schleyer, P. V.; Stoll, H.; Preuss, H. *J. Chem. Phys.* **1991**, *94*, 1360–1366.

(72) Hariharan, P. C.; Pople, J. A. *Theor. Chim. Acta* **1973**, *28*, 213–222.

(73) Hehre, W. J.; Ditchfie, R.; Pople, J. A. *J. Chem. Phys.* **1972**, *56*, 2257−2261.

(74) Scalmani, G.; Frisch, M. J. *J. Chem. Phys.* **2010**, *132*, 114110.

(75) Bowman, D. N.; Jakubikova, E. *Inorg. Chem.* **2012**, *51*, 6011−6019.

(76) Laurent, A. D.; Jacquemin, D. *Int. J. Quantum Chem.* **2013**, *113*, 2019−2039.

(77) Jakubikova, E.; Chen, W.; Dattelbaum, D. M.; Rein, F. N.; Rocha, R. C.; Martin, R. L.; Batista, E. R. *Inorg. Chem.* **2009**, *48*, 10720−10725.

(78) Bauernschmitt, R.; Ahlrichs, R. *Chem. Phys. Lett.* **1996**, *256*, 454−464.

(79) Casida, M. E.; Jamorski, C.; Casida, K. C.; Salahub, D. R. *J. Chem. Phys.* **1998**, *108*, 4439−4449.

(80) Stratmann, R. E.; Scuseria, G. E.; Frisch, M. J. *J. Chem. Phys.* **1998**, *109*, 8218−8224.

(81) Frisch, M. J.; Trucks, G. W.; Schlegel, H. B.; Scuseria, G. E.; Robb, M. A.; Cheeseman, J. R.; Scalmani, G.; Barone, V.; Mennucci, B.; Petersson, G. A.; Nakatsuji, H.; Caricato, M.; Li, X.; Hratchian, H. P.; Izmaylov, A. F.; Bloino, J.; Zheng, G.; Sonnenberg, J. L.; Hada, M.; Ehara, M.; Toyota, K.; Fukuda, R.; Hasegawa, J.; Ishida, M.; Nakajima, T.; Honda, Y.; Kitao, O.; Nakai, H.; Vreven, T.; Montgomery, J. A., Jr.; Peralta, J. E.; Ogliaro, F.; Bearpark, M.; Heyd, J. J.; Brothers, E.; Kudin, K. N.; Staroverov, V. N.; Kobayashi, R.; Normand, J.; Raghavachari, K.; Rendell, A.; Burant, J. C.; Iyengar, S. S.; Tomasi, J.; Cossi, M.; Rega, N.; Millam, J. M.; Klene, M.; Knox, J. E.; Cross, J. B.; Bakken, V.; Adamo, C.; Jaramillo, J.; Gomperts, R.; Stratmann, R. E.; Yazyev, O.; Austin, A. J.; Cammi, R.; Pomelli, C.; Ochterski, J. W.; Martin, R. L.; Morokuma, K.; Zakrzewski, V. G.; Voth, G. A.; Salvador, P.; Dannenberg, J.J.; Dapprich, S.; Daniels, A. D.; Farkas, Ö.; Foresman, J. B.; Ortiz, J. V.; Cioslowski, J.; Fox, D. J. *Gaussian 09*, Revision B.01; Gaussian, Inc.: Wallingford, CT, 2009.

(82) Kresse, G.; Furthmüller, J. *Phys. Rev. B: Condens. Matter Mater. Phys.* **1996**, *54*, 11169.

(83) Kresse, G.; Hafner, J. *Phys. Rev. B: Condens. Matter Mater. Phys.* **1993**, *47*, 558.

(84) Kresse, G.; Furthmüller, J. *Comput. Mater. Sci.* **1996**, *6*, 15.

(85) Kresse, G.; Hafner, J. *Phys. Rev. B: Condens. Matter Mater. Phys.* **1994**, *49*, 14251.

(86) Perdew, J.; Burke, K.; Ernzerhof, M. *Phys. Rev. Lett.* **1997**, *78*, 1396.

(87) Perdew, J.; Burke, K.; Ernzerhof, M. *Phys. Rev. Lett.* **1996**, *77*, 3865−3868.

(88) Kresse, G.; Joubert, D. *Phys. Rev. B: Condens. Matter Mater. Phys.* **1999**, *59*, 1758.

(89) Kabsch, W. *Acta Crystallogr., Sect. A: Cryst. Phys., Diffr., Theor. Gen. Crystallogr.* **1978**, *34*, 827−828.

(90) Rego, L. G.; Batista, V. S. *J. Am. Chem. Soc.* **2003**, *125*, 7989−7997.

(91) Abuabara, S. G.; Rego, L. G. C.; Batista, V. S. *J. Am. Chem. Soc.* **2005**, *127*, 18234−18242.

(92) Bowman, D. N.; Blew, J. H.; Tsuchiya, T.; Jakubikova, E. *Inorg. Chem.* **2013**, *52*, 14449−14449.

(93) Bowman, D. N.; Blew, J. H.; Tsuchiya, T.; Jakubikova, E. *Inorg. Chem.* **2013**, *52*, 8621−8628.

(94) Jakubikova, E.; Snoeberger, R. C., III; Batista, V. S.; Martin, R. L.; Batista, E. R. *J. Phys. Chem. A* **2009**, *113*, 12532−12540.

(95) Abuabara, S. G.; Cady, C. W.; Baxter, J. B.; Schmuttenmaer, C. A.; Crabtree, R. H.; Brudvig, G. W.; Batista, V. S. *J. Phys. Chem. C* **2007**, *111*, 11982−11990.

(96) McNamara, W. R.; Snoeberger, R. C., 3rd; Li, G.; Schleicher, J. M.; Cady, C. W.; Poyatos, M.; Schmuttenmaer, C. A.; Crabtree, R. H.; Brudvig, G. W.; Batista, V. S. *J. Am. Chem. Soc.* **2008**, *130*, 14329−14338.

(97) Bowman, D. N.; Mukherjee, S.; Barnes, L. J.; Jakubikova, E. *J. Phys.: Condens. Matter* **2015**, *27*, 134205.

(98) Dietrich-Buchecker, C. O.; Sauvage, J. P. *Tetrahedron Lett.* **1983**, *24*, 5091−5094.

(99) Miller, M. T.; Gantzel, P. K.; Karpishin, T. B. *Inorg. Chem.* **1998**, *37*, 2285−2290.

(100) Coskun, A.; Hmadeh, M.; Barin, G.; Gándara, F.; Li, Q.; Choi, E.; Strutt, N. L.; Cordes, D. B.; Slawin, A. M. Z.; Stoddart, J. F.; Sauvage, J. P.; Yaghi, O. M. *Angew. Chem., Int. Ed.* **2012**, *51*, 2160−2163.

(101) Baranoff, E. D.; Voignier, J.; Yasuda, T.; Heitz, V.; Sauvage, J. P.; Kato, T. *Angew. Chem., Int. Ed.* **2007**, *46*, 4680−4683.

(102) Dietrich-Buchecker, C. O.; Sauvage, J. P.; Kern, J. M. *J. Am. Chem. Soc.* **1984**, *106*, 3043−3045.

(103) Everly, R. M.; McMillin, D. R. *J. Phys. Chem.* **1991**, *95*, 9071−9075.

(104) Kau, L. S.; Spira-Solomon, D. J.; Penner-Hahn, J. E.; Hodgson, K. O.; Solomon, E. I. *J. Am. Chem. Soc.* **1987**, *109*, 6433−6442.

(105) Smith, T. A.; Penner-Hahn, J. E.; Berding, M. A.; Doniach, S.; Hodgson, K. O. *J. Am. Chem. Soc.* **1985**, *107*, 5945−5955.

(106) Ravel, B.; Newville, M. *J. Synchrotron Radiat.* **2005**, *12*, 537−541.

(107) Newville, M. *J. Synchrotron Radiat.* **2001**, *8*, 322−324.

(108) Johansson, M. P.; Olsen, J. *J. Chem. Theory Comput.* **2008**, *4*, 1460−1471.

(109) Löwdin, P.-O. *Phys. Rev.* **1955**, *97*, 1474−1489.

(110) Vittadini, A.; Selloni, A.; Rotzinger, F. P.; Gratzel, M. *J. Phys. Chem. B* **2000**, *104*, 1300−1306.

(111) Nilsing, M.; Persson, P.; Ojamae, L. *Chem. Phys. Lett.* **2005**, *415*, 375−380.

(112) Perez Leon, C.; Kador, L.; Peng, B.; Thelakkat, M. *J. Phys. Chem. B* **2006**, *110*, 8723−8730.

(113) Labat, F.; Adamo, C. *J. Phys. Chem. C* **2007**, *111*, 15034−15042.

(114) Hirva, P.; Haukka, M. *Langmuir* **2010**, *26*, 17075−17081.

(115) Hoff, D. A.; Silva, R.; Rego, L. G. C. *J. Phys. Chem. C* **2011**, *115*, 15617−15626.

(116) Ardo, S.; Meyer, G. *Chem. Soc. Rev.* **2009**, *38*, 115−164.

(117) Imahori, H.; Kang, S.; Hayashi, H.; Haruta, M.; Kurata, H.; Isoda, S.; Canton, S. E.; Infahsaeng, Y.; Kathiravan, A.; Pascher, T. R.; Chábera, P.; Yartsev, A. P.; Sundström, V. *J. Phys. Chem. A* **2011**, *115*, 3679−3690.

(118) Mukherjee, S.; Bowman, D. N.; Jakubikova, E. *Inorg. Chem.* **2015**, *54*, 560−569.